Extension of the TT Test Stand with a Pulsed Focused Infrared Laser

Physik-Institut der Universität Zürich

Bachelor Thesis

of

Christian Elsasser

Supervisor: Dr. Olaf Steinkamp

Abstract: The test stand at the University of Zurich for silicon micro-strip detectors used in the Tracker Turicensis (TT) of the LHCb experiment has been equipped with a movable pulsed focused infrared Nd:YAG-laser ($\lambda = 1066\,\mathrm{nm}$). This provides the possibility for testing and investigating the sensors with a simulation of incoming particles.

This thesis describes on the one hand the required extensions of the test stand which are the generating of the laser clocking signal, the control of the step motors and the supply and control of the bias voltage. On the other hand it covers first measurements performed with the laser beam as for example pulse shape measurements or investigations of the spatial resolution. For the latter issue the charge sharing coefficient η between neighboring strips was considered.

Acknowledgment

A range of people have supported me during the work on my thesis. I'd like to take the opportunity to express my gratitude towards them. First of all I want to thank my supervisor *Dr. Olaf Steinkamp*. His support as well as the numerous fruitful discussions with him were key success factors for this thesis.

Another important person for this work was *Dr. Achim Vollhardt*. His assistance on electronic issues as well as his numerous useful comments on the performance of the extensions to the test stand have successfully contributed to this thesis.

I thank also *Dr. Roland Bernet* for his help and consultancy in informatics questions, *Angela Büchler* for bailing me out of problems about PVSS, *Stefan Steiner*, who made the modifications to the step motor system, and *Dr. Mark Tobin* for his assistance on the data acquisition system as well as for writing new versions of the data processing programs.

Further I'd like to thank *Prof. Ulrich Straumann* giving me the possibility to write my Bachelor thesis in his research group.

Last but not least I want to thank all the people who supported my work in multifaceted manner.

<div align="right">

Christian Elsasser
Zurich, November 7, 2009

</div>

Contents

List of Figures

List of Tables

Introduction

The LHC*b*-experiment at *CERN* – one of the four large experiments of the *LHC* – has the goal to accumulate new data for studying *B*-physics. A part of its detector system forms the *Tracker Turicensis (TT)*. To get a possibility to examine the modules of the TT-detector outside of the experiment, a test stand was set up at the University of Zurich. Subjects of this thesis were the extension of the test stand set up by a small movable infrared laser simulating incoming particles and first measurements to characterize modules.

Outline In section 1 there is a short overview about the LHC*b*-experiment and the TT-detector in particular. Section 2 describes the extensions made to the test stand whereas the offline data processing with MATLAB is specified in section 3. The further sections contain the results of the first measurements performed with the laser: Section 4 (Pulse shape) and 5 (Focus alignment) describe measurements to adjust the front end electronics and the laser beam. Section 6 shows the signal change in strips as the laser beam is scanning over the sensor, whereas section 7 is devoted to the spatial resolution and section 8 examines so-called broken bonds and their influence on the spatial resolution. The appendices (A - D) contain among others a current version of the test stand manual and further information about the step motors used to move the laser and their control.

1 LHCb and TT-station

1.1 The LHCb-experiment

The LHC*b* experiment is designed to study rare decays and *CP*-violating processes of *B*-mesons. *CP*-violation is the phenomenon of the weak interaction that the *CP*-symmetry[1] is not conserved in certain processes.

This quality is in the standard modell usually represented by a complex phase in the unitary *CKM-matrix*, which describes the relation between the mass eigenstates of quarks and the eigenstates of weak interaction of the *d*-family quarks.

At first the *CP*-violation was discovered in relation to *K*-mesons, later it was also seen in processes involving *B*-mesons. While the *CP*-violation in the *K*-mesons is quite small, the larger violation in case of *B*-mesons as well as the higher number of decay processes, giving the possibility for consistency checks, make the *B*-mesons better candidates for the investigation of *CP*-violation [2, pp. 333 - 343], [8], [11].

As at the LHC particles containing heavy *b*-quarks are mostly produced under a small angle to the beam axis the experiment is designed as a single-arm spectrometer including different types of detectors. Fig. 1 shows the side view of the spectrometer.

The tracking system of the LHC*b*, together with the dipole magnet also able to measure particle momenta, is based on the *Vertex Locator (VELO)*, the *Tracker Turicensis (TT)* just before the dipole magnet and the three planar tracking stations T1 - T3 behind it. In the TT as well as in the region of T1 - T3 near the beampipe, named *Inner Tracker (IT)*, silicon microstrip sensors are used [1].

1.2 Silicon microstrip sensors

A silicon microstrip sensor is usually made of an n-doped – the charge carriers are primary electrons – silicon wafer. At the backside of the wafer there are an n^+-implant and an aluminium backplane while at the frontside there are p^+-strip implants producing a pn-junction (cf. fig. 2). Therefore the sensor can be considered as an extended diode.

To read out the signals there are metal strips (readout channels) just above the implants connected to the readout electronics. A thin isolating layer of silicon oxide between the implants and the metal strips decouples the readout electronics from the leakage currents. To enlarge the efficiency of the sensor a reverse bias voltage is applied between the backplane and the p^+-implants producing an expansion of the depletion volume to the whole thickness of the wafer.

---

[1]The *CP*-operator is a combination of the parity- *P* and the charge-conjugation-operator *C*, making a right- or left-handed anti-particle out of a left- or right-handed particle (i.e. $CP|\alpha_{r,l}\rangle = |\overline{\alpha}_{l,r}\rangle$).
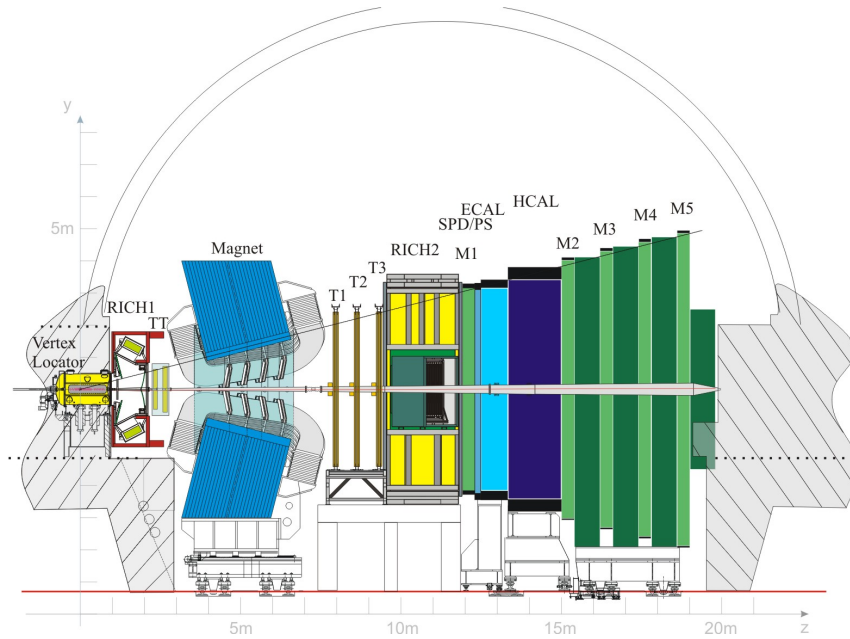
Figure 1: Side view of LHC*b* (RICH: Ring Imaging CHerenkov detector, ECAL: Electromagnetic CALorimeter, HCAL: Hadronic CALorimeter, M1-5: Muon detectors, SPD/PS: Scintillating Pad Detector/PreShower) [1]

The principle of a silicon sensor is that an ionizing particle produces in the silicon electron-hole pairs which are accelerated in the electric field of the depletion zone, traversing to the metal strips and resulting in a charge signal [10, pp. 104 - 108], [19]. The dimensions of the sensor used at the TT-station are indicated in tab. 1.

Table 1: Dimensions of a TT-sensor [21]

Length	9.44	mm
Width	9.64	mm
Thickness	500	μm
Number of p$^+$-implant strips	512	
Number of readout strips	512	
Pitch	183	μm
Width p$^+$-implant	46	μm
Width metal strip	58	μm
full depletion voltage	160-240	V

One important dimension in tab. 1 is the *pitch*, the distance between neighboring readout strips. A smaller pitch leads obviously to a more precise reconstruction of the particle track, but is also more expensive.
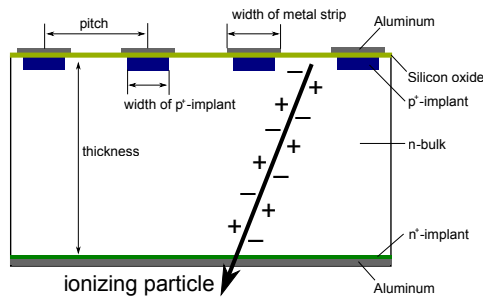
Figure 2: Scheme of a silicon sensor showing its structure and including the important properties (based on [10])
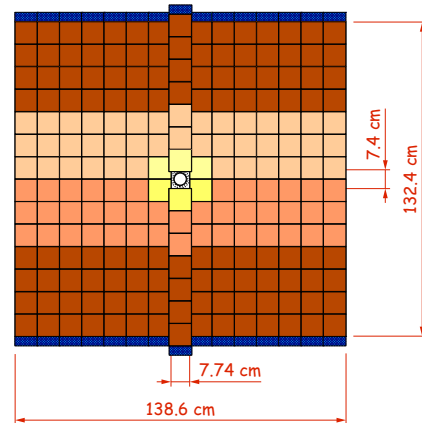
Figure 3: Scheme of one of the four TT detector planes (TTa x). It consists of 24 half-modules (12 supermodules) type 4-3 and 6 (2 supermodules + 2 single) type 4-2-1 [20].

1.3 The TT-station

At the TT-station seven sensors are mounted on support rails and form a so-called *half-module*. These half-modules build four detection planes with a surface of approximately $1.8\,\mathrm{m}^2$ each (cf. fig. 3).

There are two different types of half-modules: Around the beampipe the sensors are arranged in three readout sections with four, two and one sensor(s) (named L, M2 and K) while further away they are split into two readout sections including four and three sensors (named L and M3).

For every readout section the half-module possesses a Hybrid, carrying the front-end readout electronics. The strips are either directly (in case of the readout section L) or via a kapton cable connected to the Hybrid. Every of the 512 strips in a readout section is bonded to a pitchadapter on the Hybrid. The four Beetle chips on the Hybrid [14] process the signal of 128 strips per chip. They sample the charge signal every 25 ns to a peak signal and store it in an analogue pipeline memory. This memory contains the charge information of the last 160 samples. The Beetle reads on a trigger-accept signal the information at an exact position in the pipeline. The position is defined by the latency which is tunable at the Beetle chip or at the Readout Supervisor (*ODIN*). The signal of 32 strips is sent via one of the four output ports as analogue values with a duration of 25 ns each. Such a data packet is preceded by four binary header bits including extra information (e.g. pipeline position) so that the total length of the data per port is 900 ns [1], [18], [19].

2 Extension of the test stand

This section describes the extensions that have been made to the test stand. A schematical overview is shown in fig. 4.

2.1 Control systems and data acquisition at the test stand

The main part of the test stand is the light-tight test box. The humidity and temperature inside can be controlled by a cooling system and by flushing the box with dry air or nitrogen. The half-module (A1) to be tested is attached to a heatsink (A6) via a balcony (A5). The test stand has already been built up in an earlier thesis such that it is possible to control the front end electronics, to send trigger signals and make data acquisition [12]. All these tasks are performed by devices which can be divided in three groups:

- *Experiment Control System (ECS)* including the *Control Board* controlled by the Windows booted PC *Drache* via the *Specs Master*. The Control Board is responsible for the distribution of fast control signals to the Beetle chips and the Digitizer Boards as well as for the control of various subsystems.

- *Trigger and Fast Control (TFC)* including the *Readout Supervisor (Odin)* controlled by the Linux booted PC *Lama*. The Odin is used at the test stand for providing trigger signals.

- *Data Acquisition (DAQ)* including the *Digitizer Boards* and the *TELL1 board* controlled by the PC *Lama* and the also Linux booted PC *Kamel*. The from the analogue pipeline read out signals are sent via a copper cable (a) to the Digitizer Board where they are sampled by Analogue-Digital-Converters (ADC). The range of the digital signal is a byte, therefore the maximal raw ADC-value is 255^2. Afterwards the digital signals are brought by optical fibers to the TELL1 board. At the LHC*b* experiment the TELL1 board processes the data by doing pedestal subtraction, common mode subtraction, zero suppression and clustering (further details in section 3). These steps are skipped at the test stand and the data is transmitted to the PC *Kamel* where a TELL1 emulator processes the data [7] [19].

A target during the assembling of the test stand was to imitate the situation at the LHC*b* as far as possible. For further details see [12].

---

[2] This fact is important to recognize saturation of the detector.
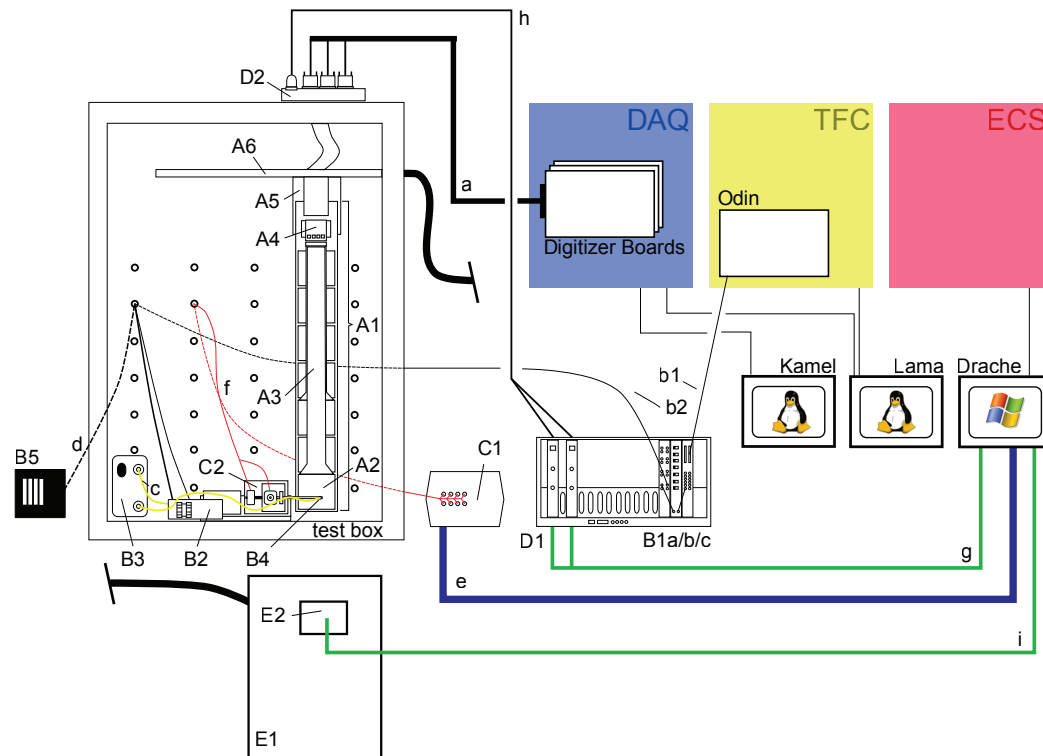
A: Test box and half-module
A1: Half-module, **A2:** Sensor, **A3:** Kapton cable, **A4:** Hybrid, **A5:** Balcony, **A6:** Heatsink

B: Laser system
B1a/b/c: Laser input signal converting NIM-modules (f.r.t.l.: ECL-NIM, Delay, NIM-TTL), **B2:** Laser amplifier, **B3:** Passive attenuator, **B4:** Collimator, **B5:** Power supply

C: Step motor system
C1: Interface box with SMC800 step motor interface card inside, **C2:** Movable structure incl. step motors

D: Bias voltage supply
D1: NIM HV-modules, **D2:** Patch panel

E: Cooling system
E1: Unichiller cooling device, **E2:** Polystat CC3

Transmission Lines:
a: Analogue Beetle data, **b1:** Orbit signal ECL (Lemo), **b2:** Orbit signal TTL (Lemo), **c:** Optical laser signal, **d:** Laser amplifier power supply, **e:** IEEE 1284 AB, **f:** current supply step motors, **g:** RS232 (HV), **h:** HV-cable, **i:** RS232 (Polystat CC3)

Figure 4: Scheme of the test stand and its transmission lines

2.2 Laser beam

The heart of the extensions made during this thesis is a pulsed and focused laser that can be used to simulate particles by creating electron-hole pairs in the silicon. The used laser is a Nd:YAG-laser[3] with spectral maximum at $\lambda = 1066\,\text{nm}$ ($\lambda_{min} = 1055\,\text{nm}$, $\lambda_{max} = 1075\,\text{nm}$, cf. fig. 5). A photon of this laser has an energy of $E_{ph} = hc/\lambda = 1.163\,\text{eV}$ [25]. The band gap in silicon at T=300 K is $E_{gap} = 1.12\,\text{eV}$ [9], so the photon energy is just sufficient to lift an electron onto the conduction band. But actually the necessary energy to create an electron-hole pair is dependent on the occupied states resulting in a mean required energy of 3.5 eV [10, p. 19]. Therefore most of the charge carriers are created in multi-photon events.
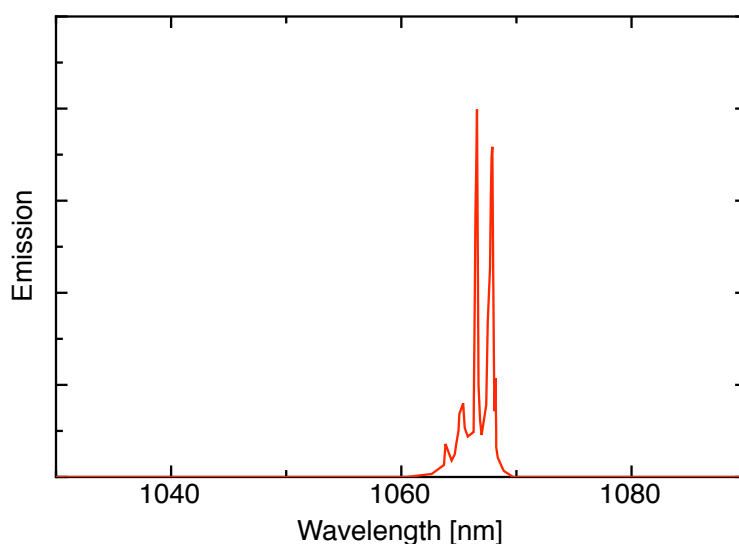
Figure 5: Emission spectrum of the used Nd:YAG-laser (based on [25])

The laser amplifier [25] is embedded in a small box (B2) together with the thermoelectric cooling controller [22], which stabilizes the temperature of the laser diode. The power supply (B5) is kept outside of the test box for lack of space. To clock the laser the ECL orbit signal of the *Readout Supervisor (Odin)*, out of connection P1-R on the Odin board, is used. As the laser amplifier needs a TTL signal, it is converted in NIM-modules (B1a/b/c), where a delay box has been set between the two conversion steps to get a further possibility to change the timing between the laser signal and the readout of the analogue pipeline. In fig. 6 the TTL pulse of the input signal to the laser amplifier is pictured.

---

[3]Neodymium-doped yttrium aluminum garnet laser
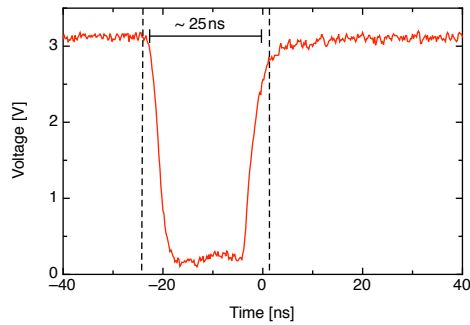
Figure 6: Plot of the pulsed TTL signal working as the clocking signal for the laser amplifier. The pulse has approximate length of 25 ns (pictured via oscilloscope).
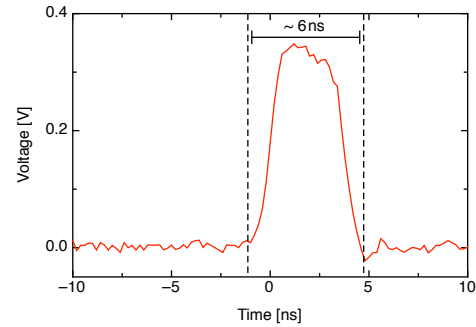
Figure 7: Plot of the laser pulse after the attenuator. The pulse was converted by a TIA-950 O/E converter (details in [27], used calibration: Gain 12'000, AC coupling) and displayed on an oscilloscope (Tektronix TDS 3034).

The output laser signal of the amplifier is first transmitted via an optical fibre (c) to a passive[4] adjustable optical attenuator (B3) to avoid a saturation of the detector readout signal. Almost all measurements were performed with an attenuation of 15.5 dB, which has been found to be enough strong to avoid any saturation.

The shape of the laser signal after the attenuator is displayed in fig. 7. The signal is again brought by an optical fibre to the collimator (B4) mounted at the tip of a metal rod belonging to the movable structure described in section 2.3. The collimator points toward the half-module and its lense system is focussing the laser signal[5].

2.3 Step motors

To be able to analyze different readout strips and take measurements as a function of the laser position between two strips, the collimator is as mentioned before fixed on a movable structure (C2). A detailed picture is in fig. 8. The structure had been already assembled for former tests of prototype modules [6]. It possesses two step motors enabling motions in a direction perpendicular and parallel to the laser beam. These directions will be referred to as x- and z-direction as indicated in fig. 9.

The collimator has to be movable along the z-axis as the laser signal is focused and therefore the distance between detector and collimator has to be chosen such that the focal point is positioned in the middle of the silicon bulk. A motion along the readout strips (y-direction) to check different sensors and readout sections is not scheduled yet.

---

[4]The attenuation level is also maintained if the attenuator is turned off.

[5]The manufacture specifies the focal distance of the collimator by 12 mm.

The two axis-motors are bipolar step motors (Tandon KP4M2-203) with two phases. The step angle is $1.8°$ which is equivalent to 200 steps per turn.

The x-axis motor moves a slider via a screw thread with lead 1 mm. Therefore the positioning precision in the x-direction is $5\,\mu$m. The z-axis motor is fixed on the slider and moves the mentioned metal rod with the collimator by another screw thread with lead 0.5 mm. Thus the precision in the focal direction is $2.5\,\mu$m [26].
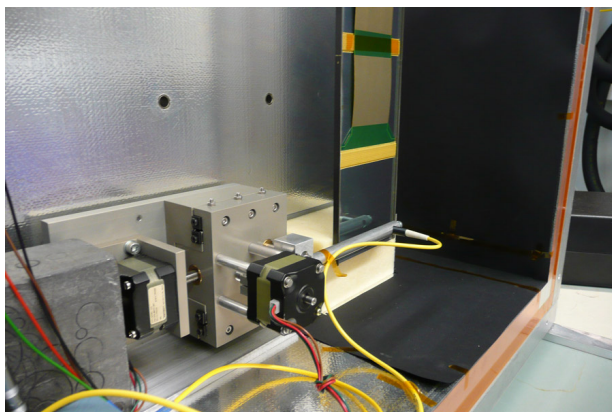
Figure 8: Photo of the movable structure including the two step motors (left: x-axis, right: z-axis) and the collimator on the metal rode. Also visible are the four wires per motor, providing the current, and the pre-tensioning plastic block behind the half-module.
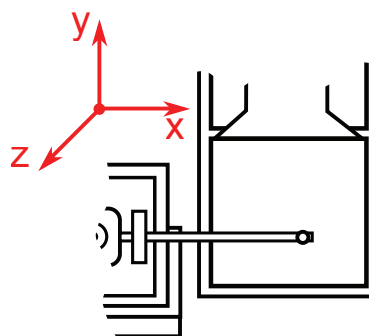
Figure 9: Notation of the axes: x-axis ("Scan") along the sensor perpendicular to the readout strips, y-axis along the readout strips, z-axis ("Focus") perpendicular to the sensor

The control of the two motors is done by a SMC800 step motor interface card placed outside of the test box (C1). As input the interface card receives a byte per step from the Windows booted PC *Drache* over its parallel port. The LabView-program `Step_con-trol.vi` on this PC provides a control panel.

Errors in the positioning reproducibility are minimized by selecting a reference direction (on both axis the positive direction). When moving to a new position, the motors perform always the last few steps in this direction making the positioning reproducible despite of backlash in the mechanical system [23].

Further details about the step motor control are written down in appendix B.

The half-module in the test box is only attached to the balcony. It can therefore easily vibrate. A pre-tensioning plastic block put between the back wall of the test box and the module inhibits these vibrations. The exact pre-tension can be adjusted by placing hard-plastic disks between the block and the wall.

Further the inner side of the test box wall near the half module is covered with black paper to avoid reflexions of the laser beam.

2.4 Bias voltage supply

To fully deplete the silicon bulk, a bias voltage between 250 and 500 V has to be applied. For the bias voltage supply there is an RS232 plug on the patch panel (D2), where also the copper cables going to the digitizer boards are connected. The correct allocation of the RS232 pins is indicated in fig. 10. The connections for the bias voltage to the sensors are the backplane and p^+-implants [3].

The bias voltage at the test stand is provided by two NIM-modules (ISEG NHQ-225M/ 6L, D1). The two modules can be controlled directly or over their RS232 interface by the LabView programs St225.vi and St226.vi on *Drache*. Current and voltage limits have to be set by hands on the modules.
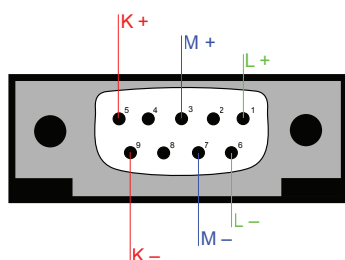
Figure 10: Allocation of the RS232 pins. In case of a type 4-3 module the connections for K are omitted.
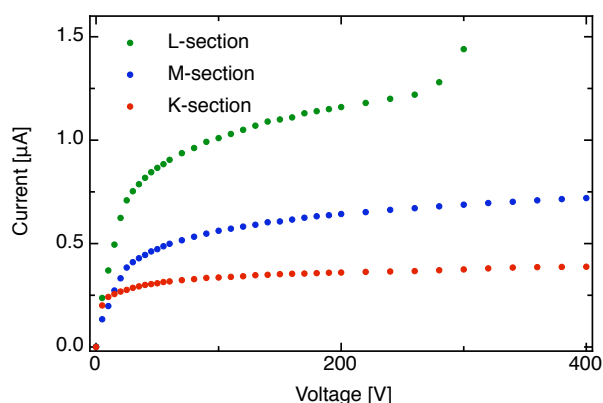
Figure 11: Plot of the IV-curve of K109, M153 and L244 (all on TT111). The proportion of the saturation currents is close to the from the length of the readout sections expected 1:2:4-ratio.

In fig. 11 the IV-curve for all three readout sections of half-module TT111 (with Hybrids K109, M153, L244) is shown. As expected from the length of the readout strips the saturation current in the L-section is approximately two times the one in the M-section, which is again two times higher than in the K-section.

For measurements the bias voltage was normally set to 300 V, which is well above the full depletion voltage of about 200 V in case of the sensors on the half-module TT111 [20, Database TT Construction Web].

2.5 Polystat control

The test stand possesses a cooling system (E1), which is responsible for temperature control of the heatsink in the testbox. The used cooling device (*Unichiller*) is controlled via the RS232 interface on its control panel (E2) by the PC *Drache*. The LabView-program `Polystat_CC3.vi` has been designed to display and control its core parameters and functions.

3 Data processing

The data acquisition draws on the analysis program *GetData* designed for the LHC*b* and using the *GAUDI* framework of the CERN to decode the ADC-values in the binary files stored from the TELL1-Board and to process them by a TELL1 emulator. This software structure is quite complicated and most of the data processing services provided by the emulator are not required for this thesis. Therefore it was decided to do the data processing offline by the MATLAB-program `GetData.m` (cf. App. C).

The latest version of *GetData* (v7r1p1) produces for this purpose, beside some histograms, also a root-file with n-tuples of the ADC-values of every readout strip event by event. The root-program `plotTuple2.C` (cf. App. C) copies the ADC-values of a selected strip as well as the values of a determinable number of neighboring strips to the left and right from the root-file to a tab-separated ASCII-file, which can be imported by the program `GetData.m`.

The program `GetData.m` performs the following steps:

Pedestal subtraction   The pedestal represents the value around which the ADC-values of all the measurements for a given readout strip without any hits fluctuate. This value may change over time and differs from channel to channel. It would also change if a different bias voltage is applied to the sensors.

To calculate it the program uses measurement runs with 60'000 or 120'000 events taken without any laser signal. These runs were always taken just before and after the actual measurement to avoid any systematical error. The program takes the mean value for every channel over all the events in these runs and stores them as pedestal p_i.

Signal calculation   The signal on a strip s_i is calculated by taking the mean value per strip over all events μ_i and subtracting the corresponding pedestal value p_i.

$$s_i = \mu_i - p_i \tag{1}$$

20

Rms calculation   To get a certain information about the variations in the measurements, the program calculates the standard deviation σ_i of the ADC-values per strip over all events:

$$\sigma_i = \sqrt{\frac{\sum_{j=1}^{n} (a_{i_j} - \mu_i)^2}{n}} \tag{2}$$

where a_{i_j} is the ADC-value of the i$^{\text{th}}$ channel at the j$^{\text{th}}$ event and μ_i is the mean value of the i$^{\text{th}}$ channel.

Since the root-program `plotTuple2.C` only writes the ADC-values of the selected channels down in the ASCII-file (lack of memory), the MATLAB-program is unable to perform any common mode subtraction.

The MATLAB-program finally returns two m-dimensional vectors where m is the number of considered channels, one containing the signal and one the rms per strip.

All measurements covered in the following sections were performed with the readout section K of the half-module TT111. If nothing else is mentioned a measurement run includes 10'000 events.

4 Pulse shape

4.1 Measurement and analysis

In a first step the pulse shape of a channel was studied to adjust the signal sampling time of the Beetle chip to the peak of the detector signal.

The laser was positioned over channel 315 just to the right of the metal strip. A coarse focussing was done by the method described in section 5.1.

The change of the latency was performed by altering the parameter `Periodic Trigger A Offset` in the Readout Supervisor. It changes the time difference (latency) between the orbit signal and the sampling time by a whole number of clock cycles (≈ 25 ns).

The pulse shape measurement was taken over eight clock cycles from an offset of 155 to 163 ($\Delta t \approx 200$ ns). Within each clock cycles, linear steps of 0.5 ns were chosen taking advantage of the delay box[6]. A clock cycle is rather a little bit smaller than 25 ns (Bunch crossing frequency: 40.08 MHz). Therefore the first interval after a full clock cycle is also smaller than 0.5 ns.

These measurements were performed in contrast to any other one with an attenuation of 13.5 dB (instead of 15.5 dB), but there were no saturation effects visible in the data. The pulse shapes for channel 315 and its adjacent channels are displayed in fig. 12.

To describe the main pulses the empirical function

$$f(t) = A_0 \cdot e^{-(t-t_0)/\tau} \left(\frac{(t-t_0)^2}{2\tau^2} - \frac{(t-t_0)^3}{6\tau^3} \right) \tag{3}$$

based on the design of the CR-RC-shaper[7] in the Beetle chip has been taken [15], [17, pp. 134 - 139].

The pulse on channel 315 was fitted to the function between 15 ns and 85 ns while at the adjacent channels only the interval 15 ns to 75 ns was taken. The resulting parameters are listed in tab. 2.

Table 2: Fitted parameters of $f(t)$ on main pulses

Parameter	Channel 314	Channel 315	Channel 316
A_0	93.5 $\pm$1.2	862 $\pm$4	140.8 $\pm$1.7
τ [ns]	17.78$\pm$0.18	27.72$\pm$0.12	18.79$\pm$0.16
t_0 [ns]	11.12$\pm$0.29	12.33$\pm$0.16	11.95$\pm$0.26

---

[6]A larger delay decreases the latency!

[7]The shaper has two CR-elements followed by two RC-elements.

A characteristic quantity of the pulse relevant for operation at the LHC is the so-called *remainder r*:

$$r = \frac{f(t_{max} + 25\,\text{ns})}{f(t_{max})} \tag{4}$$

It indicates how much of the signal amplitude remains 25 ns after the maximal signal level, which is the time when the next event (i.e. bunch crossing) at the LHC would occur. This value was determined for channel 315 from the graph and is:

$$r = (49.63 \pm 0.12)\,\%$$

The measured remainder during the Burn-in tests for this Beetle chip was $(38.67 \pm 1.22)\,\%$, but this value was determined using the internal test pulse of the Beetle chip as well as applying a higher bias voltage [20, Database TT Construction Web].

Two further characteristic quantities are the *peak time* $t_p = t_{max} - t_0$ and the *rise time* $t_r = t_{90\%} - t_{10\%}$. For channel 315 they are, derived from the fitted function:

$$t_r = 21.6\,\text{ns}$$

$$t_p = 36.2\,\text{ns}$$

4.2 Adjusting the latency

The signal level of channel 315 reaches its maximum at time $t_{max} = 48.53\,\text{ns}$ – a latency of 155 clock cycles corresponds to $t = 0$. To adjust the latency, the default value of parameter `Periodic Trigger A Offset` has been set to 156. The remaining 23.5 ns were corrected by setting the parameter `TTCrx_FineDelay2` to 0h1C[8].
The adjustment has been integrated in the PVSS-library `STCommonLibs/StConstantLib.ctl` by changing `CLOCK_DES1_FINE_DELAY` and `CLOCK_DES2_FINE_DELAY` to 226 [5].

4.3 Undershooting

In fig. 12 the signal of the central channel has not returned to zero after 200 ns. To get more information about the length of this undershooting, a second measurement was performed with the laser hitting the sensor again just to the right of the readout strip of channel 315. The pulse height was measured from a latency of 154 to 194 cycles (new

---

[8]The appendix of [5] contains a conversion table for this parameter.
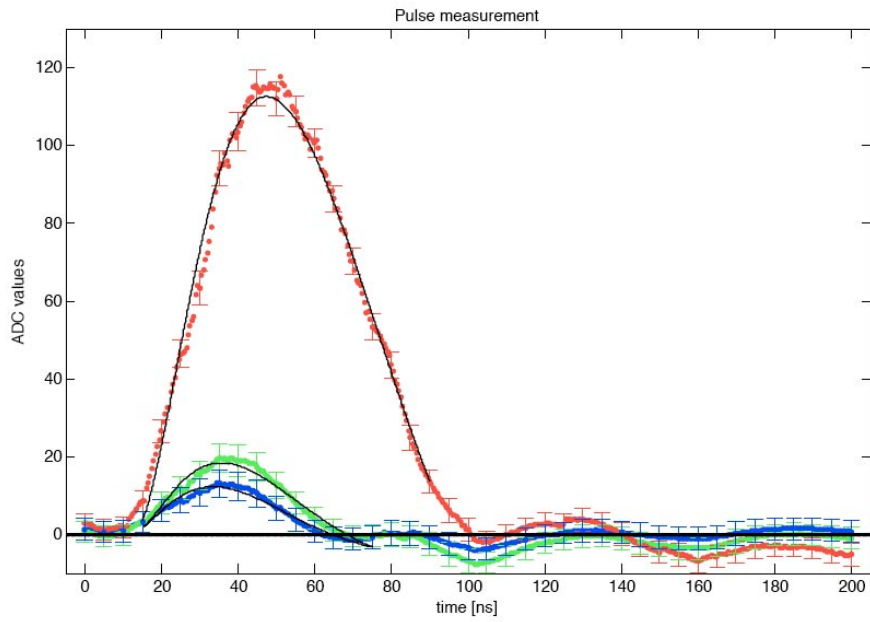
Figure 12: The figure shows the pulses measured in 0.5 ns intervals inclusive their fit functions describing the main pulse. The red plot represents Channel 315 while the blue one is 314 and the green one 316. The signal reaches its maximum faster on the neighboring strips as well as it turns back to zero earlier.
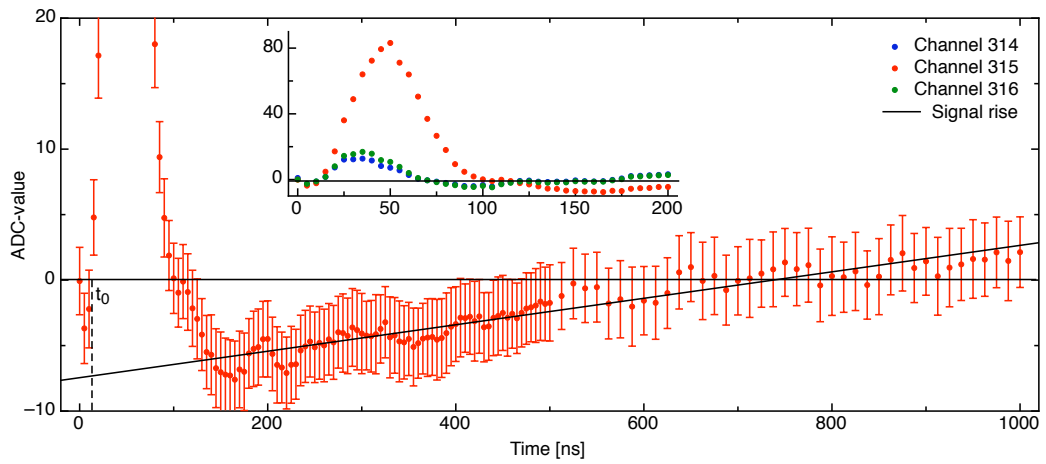
Figure 13: Long time pulse shape measurement. The black line in the rising tail represents the fitted function $f(t) = a_0 + a_1 t$. The small plot shows the pulses on the central channel and its neighbors over the first 200 ns.

24

latency adjustment in the PVSS-library). Over the first 500 ns the time intervals selected by the delay box were 5 ns, over the remaining 500 ns they were 12.5 ns long.

The data is displayed in fig. 13. A linear regression $f(t) = a_0 + a_1 t$ between 200 and 1'000 ns was done to describe the return of the signal to zero resulting in the parameters in tab. 3.

Table 3: Fitted parameters of $f(t)$ on main pulses

Parameter	
a_0	-7.5 $\pm$0.6
a_1 [ns^{-1}]	$(1.01\pm0.12)10^{-2}$

The signal reaches the zero level approximately 720 ns after $t_0 = 10.43$ ns. So the whole signal pulse including the undershooting lasts on the main channel for about 30 clock cycles.

5 Focus alignment

5.1 Principle

As mentioned above the laser beam is focused by the collimator. To get a sharp beam profile in the sensor, the focal point has to be positioned in the middle of the silicon bulk. The easiest way to do this is by taking advantage of the readout strips: The laser beam can not penetrate the aluminum strip, so if the laser beam is shining on the strip there will be no or just a small signal. Therefore if the laser beam scans across the sensor, there will be jumps of the ADC-value as the laser moves into or out of the shadow of the aluminum. The better the focus is the less steps these changes will last for a better focus corresponds to a narrower laser profile. Another indication for a good focal point is the number of steps in x-direction during which the laser is in the shadow of the aluminum. A good focus is up to more than eight of such steps ($> 40\,\mu$m; width of aluminum strip: $58\,\mu$m).

The second method can be used to get a coarse focussing. This alignment can be easily done by displaying the ADC-values of the accordant port via a DAC on an oscilloscope. For the fine focussing it is inevitable to make a range of measurements with different distances between collimator and sensor to select the z-coordinate where the ADC-value has the steepest drop-down in the scan.

5.2 Measurement

The measurements to align the focussing included fifteen scans over $200\,\mu m$ in the x-direction (40 steps) with z-coordinates from -$100\,\mu m$ to $100\,\mu m$ (smaller intervals near zero). The point $z = 0\,\mu$m has been set by a coarse focussing as described above and represents the estimated focal distance. The whole procedure has been done once at channel 281 and once at channel 315. These two channels are separated by 6.25 mm (1'250 steps) which gives an indication if the x-axis and the sensor are parallel: The coarse focussing has given a difference of $\Delta z_{fp} = z_{fp,315} - z_{fp,281} = +150\,\mu$m between the focal distance of channel 281 and 315. This would correspond to an angle of about $1.4°$ between the x-axis and the sensor.

Fig. 14 and 15 (values for strips 281 and 282) as well as 16 and 17 (values for strips 315 and 316) show the measured ADC-values for all the scans ("Scan" corresponds to the x-axis; "Focus" to the z-axis). At channel 281 and 315 the metal strip causing lower signals is very well visible. It is observable that the drop down gets – as expected – smoother towards $z = \pm 100\,\mu$m. A detailed analysis of the focal point position is done in section 5.3. The contour plots in fig. 18 and 19 show the changing of the drop down much better.
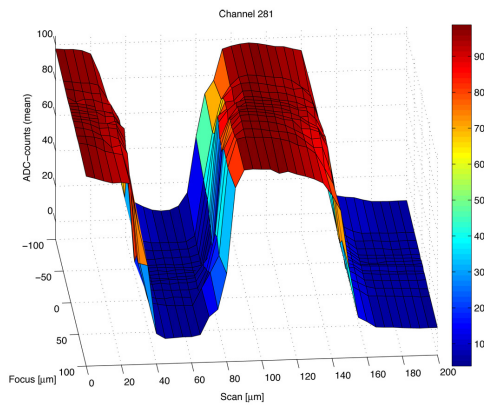
Figure 14: Signal on channel 281 plotted versus the laser position in x-direction ("Scan") and z-direction ("Focus"). The left area with small ADC-values corresponds to the aluminum readout strip which can not be penetrated by the laser beam. The right area represents the zone of charge sharing as the beam moves to channel 282.
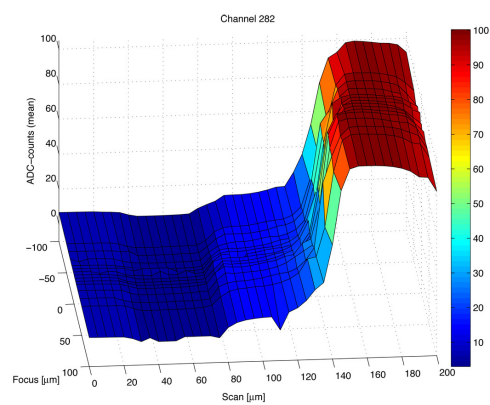
Figure 15: Signal on channel 282 plotted versus the laser position. The rise of the ADC-values to the right corresponds to the zone of charge sharing as the beam moves over from channel 281. The shadow caused by the readout strip on channel 281 is due to crosstalk also apparent with slightly smaller ADC-values around $x = 60\,\mu$m.
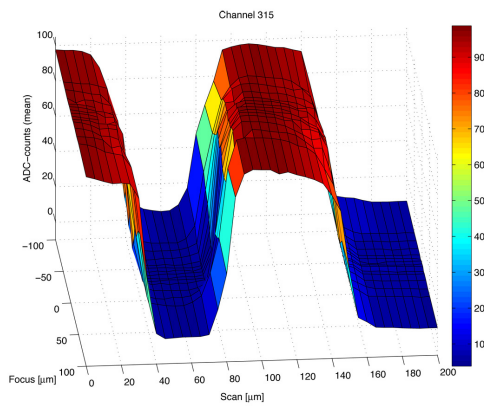
Figure 16: Signal on channel 315 plotted versus the laser position in x-direction ("Scan") and z-direction ("Focus"). The same remarks hold as for fig. 14

Figure 17: Signal on channel 316 plotted versus the laser position. The same remarks hold as for fig. 15

27
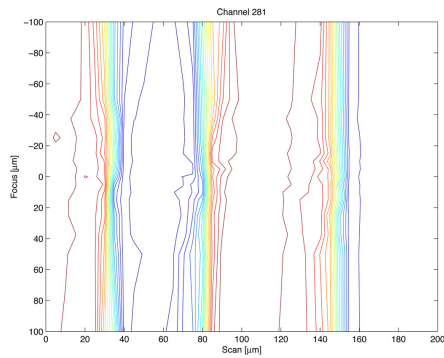
Figure 18: Signal on channel 281 plotted versus the laser position in x-direction ("Scan") and z-direction ("Focus") as a contour plot. The left and middle bundle of lines belong to the edges due to the aluminum strip, the right one to the passage of the laser beam to the higher channel.
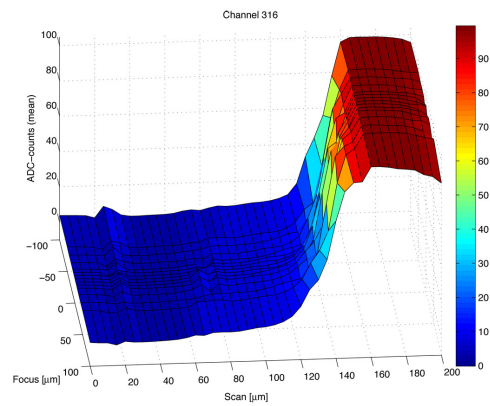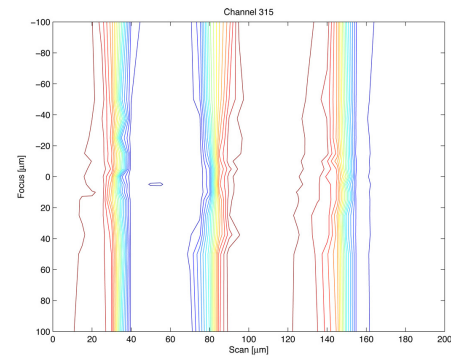
Figure 19: Signal on channel 315 plotted versus the laser position as a contour plot. The change of the focussing is more articulate as the lines in the left and middle bundle are nearer to each other around $z = 0\,\mu$m than at $z = \pm100\,\mu$m.

In the surface plots at $x > 140\,\mu$m one sees also the changing of the signal to the next higher channel as more and more charge carriers are brought by the electric field in the sensor to this channel. Later measurements will show that this transition is much smoother if the focal point is not at the surface but in the middle of the bulk due to the characteristic of the electric field.

An other quality of the sensors is a certain crosstalk between neighboring channels. There are two types of crosstalk: The first one is due to the capacitive coupling between neighboring readout strips on the sensor. Because of the geometry of the sensor this crosstalk is assumed to be symmetric. The second one is caused by the front end electronics on the Beetle readout chip, which may cause an asymmetric crosstalk [16].
In the surface plots of the next higher channels (282 and 316) this crosstalk can be seen as the ADC-value decreases while the laser is in the shadow of readout strip 281 and 315 respectively. The same is observable on strip 280 and 314 but with lower intensity pointing to an asymmetric crosstalk. To both sides the crosstalk is even noticeable on the strips after the next one. There are further discussions about crosstalk in sections 6 and 8.

Further in fig. 20 and 21 the sum of the ADC-value over the channels 280-283 and 314-317 for the charge sharing zone is plotted. The sum is quite constant except in the area where the signal switches to another channel; here the sum increases. But the hump is not constant along the z-coordinate. It decreases from $z = +100\,\mu$m to about $z = -70\,\mu$m and then increases again. This effect will be further discussed in section 6.2.

28
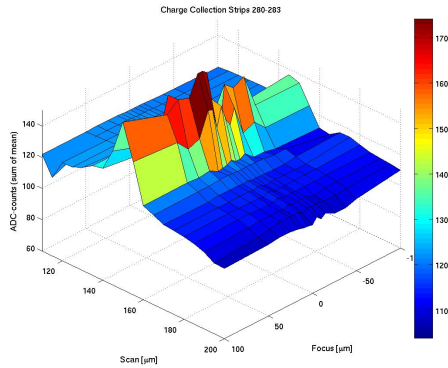
Figure 20: Plot of the summed ADC-value of channel 280 to 283 depending on x- and z-coordinate. Over the zone between the two central channels there is a crest. Its height depends on the z-coordinate and has a saddle point near $z = -70\,\mu$m (cf. fig. 22). If the laser is not between the two channels the sum is quite constant.
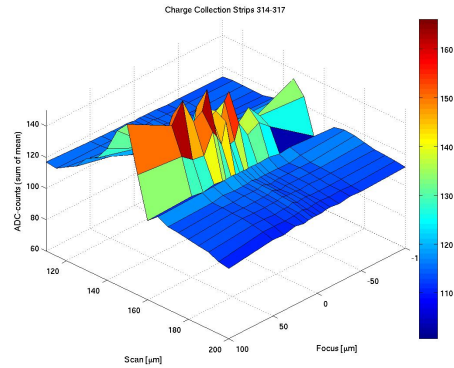
Figure 21: Plot of the summed ADC-value of channel 314 to 317 depending on x- and z-coordinate. The creast has also a saddle point near $z = -70\,\mu$m (cf. fig. 23). There is no plausible explanation about the trench to the right of the crest.
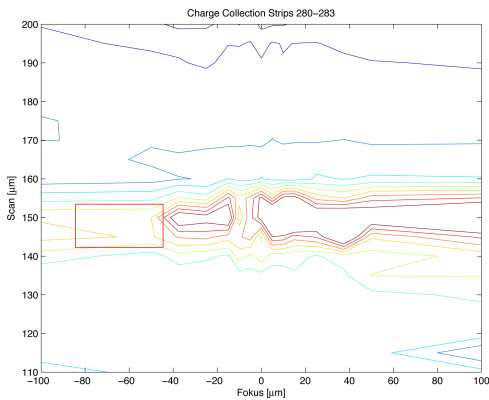
Figure 22: Contour plot to fig. 20. The saddle point is indicated by the red rectangle.
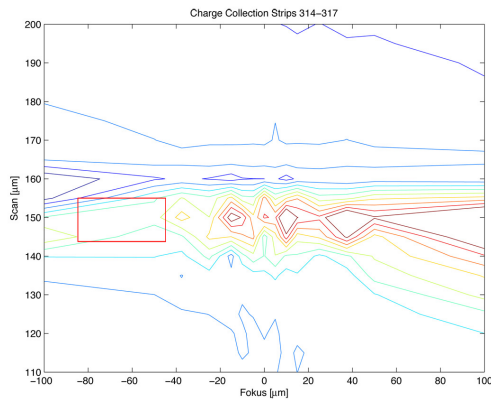
Figure 23: Contour plot to fig. 21. The saddle point is indicated by the red rectangle.

5.3 Analysis

The goal of this section is to extract from the measured data the correct distance between collimator and sensor such that the focal point lies just on the surface of the sensor.
The data points in the area of the drop down for each scan can be described (depending if it is the left or right edge of the metal strip) by the functions:

$$f(x) = a_L \cdot \left(1 - \text{erf}\left(\frac{x - \mu_L}{\sqrt{2}\sigma_L}\right)\right) + b_L \text{ (left edge)} \tag{5}$$

$$f(x) = a_R \cdot \text{erf}\left(\frac{x - \mu_R}{\sqrt{2}\sigma_R}\right) + b_R \text{ (right edge)} \tag{6}$$

Two such fits are shown in fig. 24 and 25.
A smaller σ indicates a better focussing (steeper drop down), while μ indicates the position of the edge in x-direction. a and b depend only on the total intensity of the laser beam respectively on the noise and are as expected almost constant over the different z-positions.
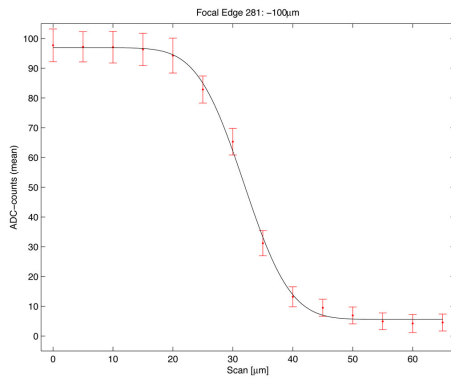
Figure 24: ADC-values in x-direction at $z = -100\,\mu$m over the left edge of the aluminum strip of channel 281. The fitted curve is the function (5).
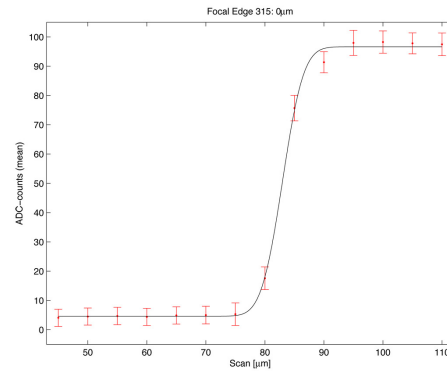
Figure 25: ADC-values in x-direction at $z = 0\,\mu$m over the left edge of the aluminum strip of channel 315. The fitted curve is the function (6). The drop down is faster as in fig. 24. Therefore the distance between collimator and sensor is nearer to the focal length.

Spot size (σ)   In fig. 26 the values of σ for the left edge of channel 281 are plotted against the z-position of the corresponding scans. By considering the beam geometry (cf. fig. 28) σ depends on z as:

$$\sigma(z) = s_1|z - s_0| + s_2 \tag{7}$$
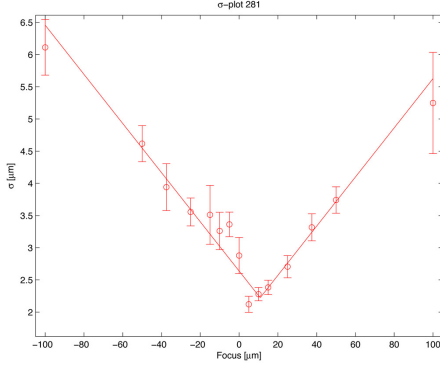
Figure 26: Plot of σ (channel 281, left edge) versus z-coordinate including the fit of form (7).

Figure 27: Plot of μ (channel 281, left edge) versus z-coodinate including the fit of form (8)

The values of $s_{0,1,2}$ for the different drop downs are recorded in tab. 4. s_0 indicates the z-coordinate of the focal point, while s_2 is a measure for the minimal reachable spot size.

Table 4: Fitted parameters of $\sigma(z)$

	Channel 281		Channel 315	
Parameter	left	right	left	right
s_0 [μm]	10.8 ± 1.8	13.2 ± 26.8	-3.1 ± 3.0	-1.1 ± 4.9
s_1	$(3.8 \pm 0.3)\,10^{-2}$	$(4.3 \pm 3.4)\,10^{-2}$	$(4.4 \pm 0.8)\,10^{-2}$	$(4.2 \pm 1.1)\,10^{-2}$
s_2 [μm]	2.2 ± 0.1	3.0 ± 0.1	2.6 ± 0.2	3.1 ± 0.3

Discussion: At both channels the positions of the focal point calculated from the left and right edge correspond. Together with the difference due to the initial coarse focussing the z-coordinates of the focal points differ between channels 281 and 315 by about $\Delta z_{fp} = z_{fp,315} - z_{fp,281} \approx +135\,\mu$m.
The opening angle of the laser beam can be estimated by $\alpha = 2\tan^{-1} s_1$ leading to a value of $\alpha \approx 5°$.
The fitted parameters show further that the σ at the focal point is about $3\,\mu$m, meaning

that at the focal point about 95% of the laser beam is inside a circle with a diameter of $4\sigma = 12\,\mu$m.

The reconstructed position of the edge (μ) The reconstructed position μ of the edge (fig. 27 shows it for the left edge on channel 281) should not depend on z if the z-axis is perpendicular to the surface of the sensor. A straight line was fitted to the data points of μ (results in tab. 5):

$$\mu(z) = m_0 \cdot z + m_1 \tag{8}$$

Table 5: Fitted parameters of $\mu(z)$

Parameter	Channel 281		Channel 315	
	left	right	left	right
m_0	$(-1.0\pm1.3)\,10^{-2}$	$(5.3\pm8.1)\,10^{-3}$	$(5.6\pm9.4)\,10^{-3}$	$(-1.2\pm6.8)\,10^{-3}$
m_1 [μm]	33.1 ± 0.2	82.1 ± 0.2	32.9 ± 0.2	82.3 ± 0.2
angle [°] ($\tan^{-1}m_0$)	-0.6 ± 0.7	0.3 ± 0.5	0.3 ± 0.5	-0.1 ± 0.4
t-test value of hypothesis $m_1 \neq 0$ (d.o.f: n=13) [level of sig.]	0.769 [<80%]	0.654 [<75%]	0.595 [<70%]	0.176 [<55%]

Discussion: The difference between m_1 on the left and right side should give an approximate value of the readout strip width. Actually the difference is at both channels about 50 μm.

The reconstructed values for m_0 and therefore the angles are compatible to zero. Furthermore, a difference of m_0 from zero is in none of the four cases statistically significant. Therefore the hypothesis that the z-axis is perpendicular on the sensor is statistically compatible to the measurements.

After these measurements the laser was set to the correct focal distance. As the focussing has been performed with respect to the strips at the sensor surface, the focal point has to be moved 250 μm inside the sensor to focus the beam in the middle of the silicon bulk. The focal point moves in the silicon bulk while the laser is moving in the air. Therefore one has to take the different refractive indices into account ($n_{Si}(\lambda = 1069\,\text{nm}) = 3.55$ [28]) resulting in a necessary motion of the collimator of only 70 μm $\approx 250/3.55\,\mu$m (cf. fig. 28). This fact had not been regarded in the measurement over a port switch and led to unexpected qualities of the charge collection (see section 6).
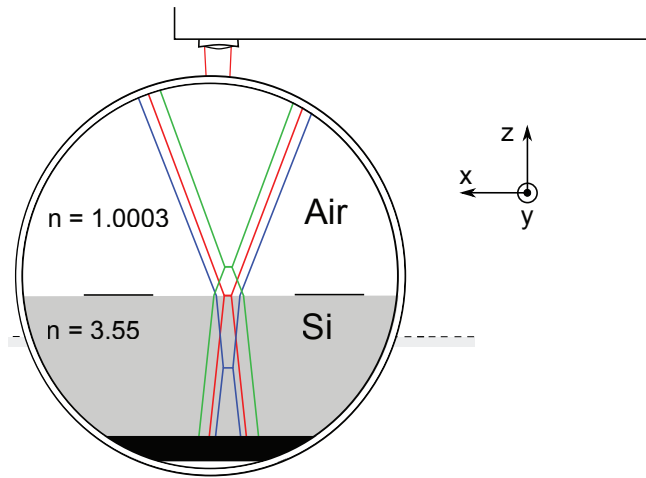
Figure 28: The drawing shows the laser ray run for three different z-coordinates. As the focal points are extended they are represented by the waist of the rays. The difference in z-coordinate of the laser between the blue and the red situation is the same as between the red and the green adjustment (compare distance of the rays in air). Anyhow the distance between the focal points are not the same: A smaller motion in the z-coordinate has to be done if the focal point should be moved over the same distance in silicon as in air.
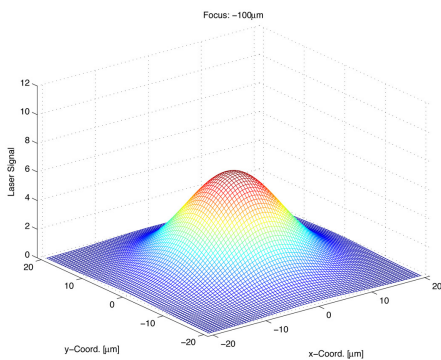
Figure 29: Laser profile at $z = -100\,\mu$m reconstructed from the ADC-values over the right edge of the readout strip 315. As the beam is not very well focused, the profile is broad.
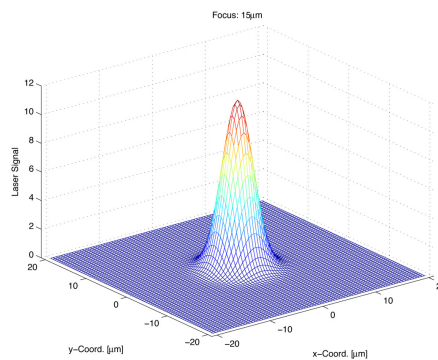
Figure 30: Laser profile at $z = +15\,\mu$m reconstructed from the ADC-values over the left edge of the readout strip 281. The profile is sharp as a result of a better focussing than in fig. 29.

5.4 Reconstruction of the laser beam profile

A two-dimensional laser beam profile was reconstructed, assuming it to be axially symmetric. As the ADC-value is proportional to the integrated beam intensity over the uncovered sensor area, the one-dimensional profile is the derivative of the measured ADC-value curve, leading to a gaussian profile. This leads finally to a two-dimensional gaussian profile:

$$f(x, y) = \frac{a}{\sqrt{2\pi}\sigma} e^{-(x^2 + y^2)/2\sigma^2} \tag{9}$$

The LabView-program `plot_profile.m` (see appendix C) allows to calculate the beam profile from a scan of measurements in x-direction.
Two calculated laser beam profiles are shown in fig. 29 and 30: The beam near the focal distance ($z = +15\,\mu$m) has obviously a narrower profile than the one at $z = -100\,\mu$m.

6 Profile measurements

6.1 Common strip

To get an idea how a readout strip reacts to the laser signal hitting on neighboring strips or on the strip itself a scan over $125\,\mu$m (250 steps) along the x-axis was taken. In fig. 32 the mean- and rms-value of the signal for channel 315 are plotted as a function of the x-position of the laser. The rms-value jitters around a value of 3 ADC-counts whereas it gets higher at very high mean-value and jitters more. This effect comes from the additional variations due to the laser beam, while the rms-value in case of no laser signal is caused by the electronic noise.

The signal shows an asymmetric behavior (cf. fig. 31): The laser beam hitting lower channels leads to higher crosstalk (The shoulder of the left main peak is higher than that of the right one.). Therefore even the aluminum strip of channel 313 is clearly visible in the red plot just below $|x| = 400\,\mu$m. That asymmetry in the crosstalk corresponds to the expected asymmetric behavior of the Beetle (electronic) crosstalk: Even channels show higher crosstalk on succeeding channels, odd channels show higher crosstalk on preceding [16].
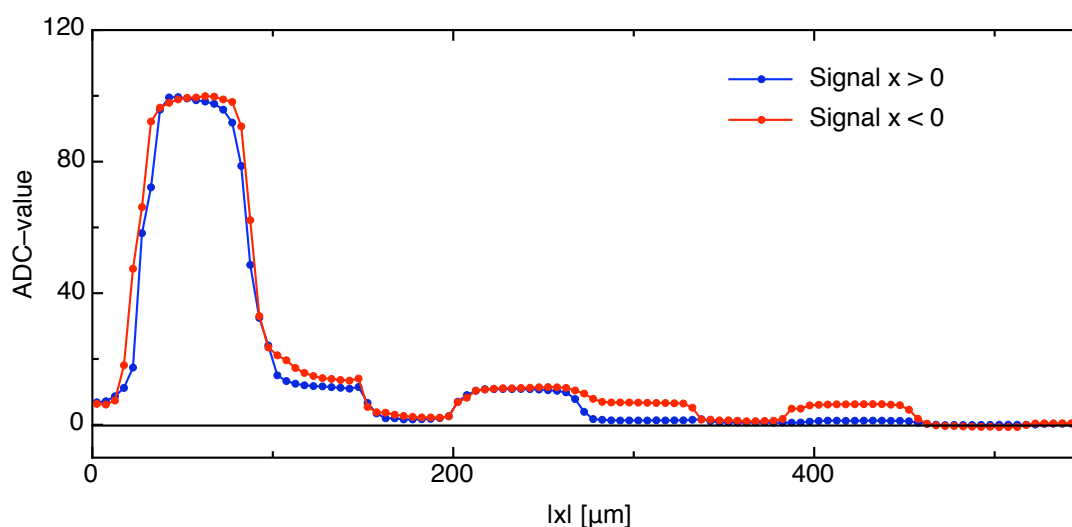
Figure 31: The plot shows the mean-value of the signal as the laser beam is to the left of the readout strip (red curve) and to the right (blue curve). The abscissa shows the absolute distance between the laser beam and the center of readout strip 315.
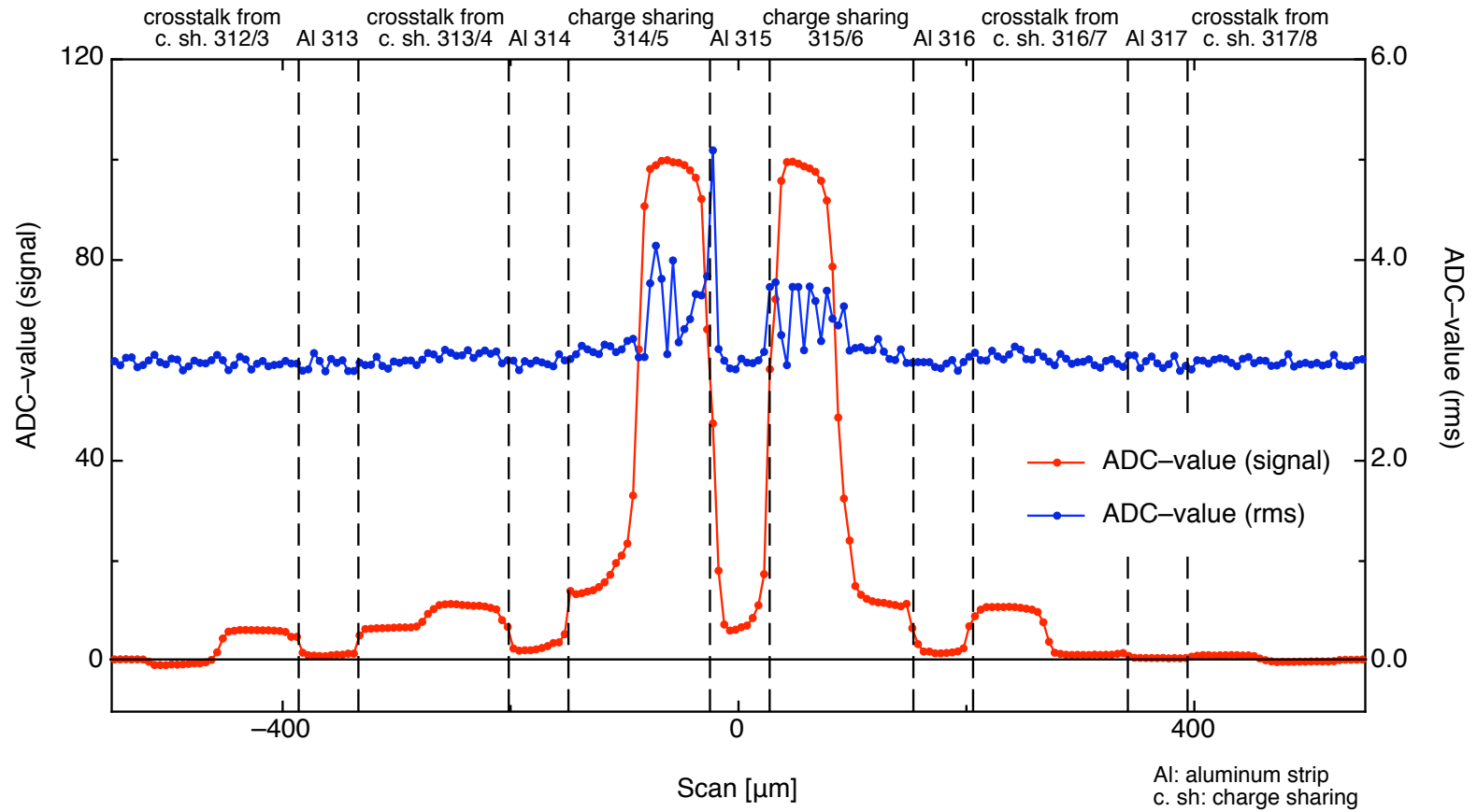
Figure 32: The plot shows the dependency of the readout signal on channel 315 on the position x of the laser beam (left axis: mean-value, right axis: rms-value). $x = 0$ refers to the middle of the strip 315. Very high ADC-values correspond also to an enhanced rms-value. The labels at the top indicate the reason for the characteristic of the signal.

6.2 Charge sharing

In charge sharing processes, as the laser beam hits the sensor in between two strips, it is assumed that there would be an incomplete collection of the charge carriers, leading to a trench in the sum of the ADC-values of the two strips at the charge sharing zone. This incomplete collection until the sampling time could be explained by the characteristic of the electric field: Not all electric flux lines run to the two p$^+$-implants but to the sensor surface in between. Therefore the charge carriers are brought to the silicon oxide layer where they may be trapped.
Previous measurements predicted that the expected incompleteness of charge collection should be the smaller the higher the reverse voltage is.

To check the prediction and the influence of the bias voltage, a set of measurements was done, involving runs over the charge sharing zone between channel 315 and 316 with 100, 200, 300 and 400 V. The latency was untouched and stayed on a level giving a maximal signal for 300 V. The resulting sums of the ADC-values of 315 and 316 and 314 to 317 are displayed in fig. 33.
An increase of the bias voltage led only to higher ADC-values below 200 V. The missing of an increase above 200 V could be also partly caused by the not adjusted latency. The measured full depletion voltage for the considered sensor is about 200 V.
Further there is no expected trench visible over the charge sharing zone, there is rather a hump at higher voltage. So there is no indication of an incomplete charge collection. But this observation will be subject of further investigations.
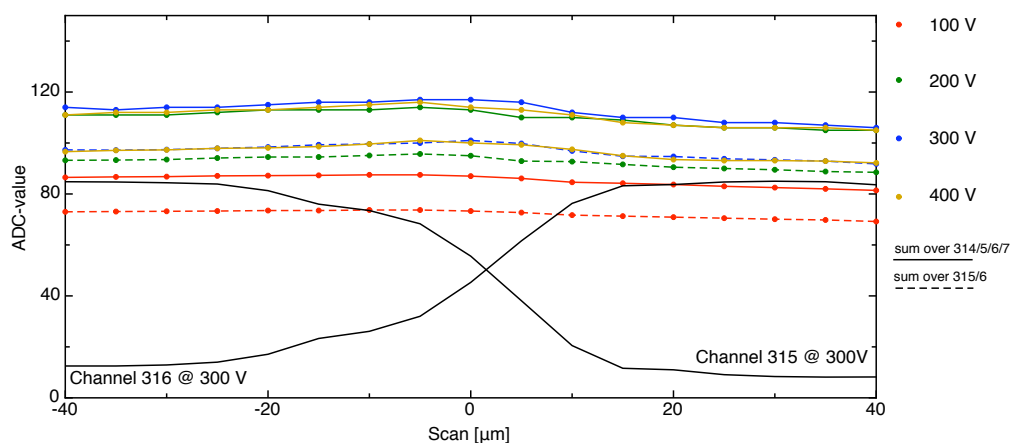
Figure 33: Plots of the sums of the ADC-values over channel 315 and 316 as well as over 314 to 317 for bias voltages of 100, 200, 300 and 400 V. $x = 0$ is in the middle between strip 315 and 316. Above 200 V an increase of the voltage does not lead to a significantly higher signal. This is partly caused by the not adjusted latency. To see the charge sharing zone, the profiles of channel 315 and 316 at 300 V are displayed.

6.3 Port switch – Header crosstalk

A second scan was made over an area where the readout strips do not belong to the same Beetle output port (Switch from port 1 to port 2 on Beetle 2, cf. section 1.3). Because the signal of the last readout strip on port 1 is in the Beetle data output stream not directly followed by the signal of the first readout strip belonging to port 2 but by four pseudo-binary header bits, there may exist an electronic crosstalk from these bits on the readout signal before and after them, called *header crosstalk* [4]. Fig. 34 displays the signal of the two last channels on port 1 and the first two channels on port 2, fig. 35 shows the associated rms-value.

Beside the already mentioned higher rms-value when the laser beam hits the strip, the channels directly followed or preceded by the header bits show increased rms-value of about 1 (Channel 319) and 0.6 (Channel 320) ADC-counts. This is probably a result of the header crosstalk.
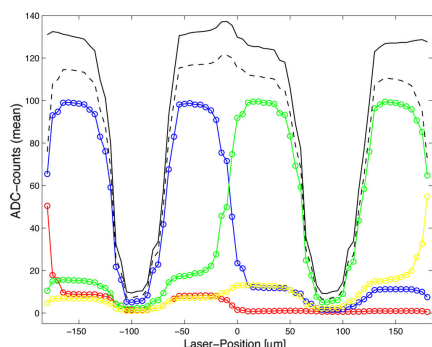
Figure 34: Signal of readout channel 318 (red), 319 (blue), 320 (green) and 321 (yellow) versus the laser position x. $x = 0$ is in the middle between strips 319 and 320. Between channel 319 and 320 there is a switch of the Beetle port. The solid black line shows the sum of the ADC-values over all four strips, the dashed one the sum over 319 and 320.
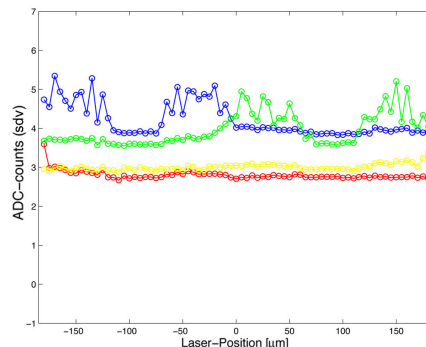
Figure 35: Rms-value of readout channel 318 (red), 319 (blue), 320 (green) and 321 (yellow) versus the laser position x. $x = 0$ is in the middle between strips 319 and 320. Channel 319 and 320 feature higher rms-values as they are directly succeeded or preceded by header bits.

Over the charge sharing zone between strip 319 and strip 320, there is a clear hump. This scan was taken in contrast to those described in section 6.2 with the wrong focussing, meaning that the laser was moved $250 \, \mu\text{m}$ toward the sensor after the focal point was placed on the sensor surface which put the focal point even behind the back plane.

The conclusion is that the summed ADC-values at the charge sharing zone do not only depend on the applied bias voltage but also hardly on the laser beam profile.

7 Spatial resolution

7.1 Principle

To reconstruct particle tracks and determine the particle momentum with high precision a good spatial resolution is indispensable.

The easiest way to define where a particle passed the sensor is to set the corresponding coordinate equal to the coordinate of the readout strip showing the main signal. Assuming that the particles hit the sensor uniformly distributed, the spatial resolution is $r = p/\sqrt{12}$ where p is the pitch. At the TT-station this gives a binary spatial resolution of about 53 μm.

So a smaller pitch gives a better resolution but implicates also a sensor design with more readout channels.

The method studied in this section uses the charge sharing between neighboring strips. For this the *charge sharing coefficient* η is applied:

$$\eta = \frac{A_{i+1} - A_i}{A_{i+1} + A_i} \tag{10}$$

A_j is the ADC-value on the j$^{\text{th}}$ strip. Only signal on the higher strip would give $\eta = 1$, only signal on the lower one $\eta = -1$.

7.2 Measurements

A first scan over two strips (315 and 316) has been performed to calculate η for every position of the laser beam. The ADC-values of this scan are shown in fig. 36. Far away from the charge sharing zone, the ADC-values are only slightly changing. Therefore there will be little spatial dependency of η. On the other hand, η increases much from step to step at the charge sharing zone. It is expected that the reconstruction of the position will be more precise where $|d\eta/dx|$ is large.

The values of a second scan over the selected strips have the goal to reconstruct the laser beam position, event by event, with the aid of η. By comparing the reconstructed to the actual position over all the events there will be an estimated value for the spatial resolution.
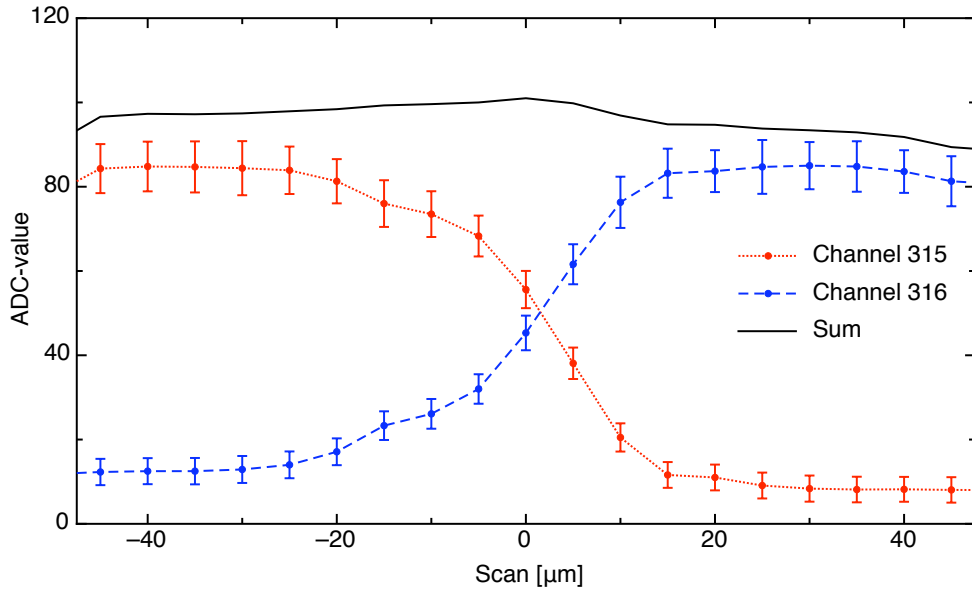
Figure 36: Plot of the ADC-values of channel 315 (red dotted line) and 316 (blue dashed line) as well as their sum (black solid line).

7.3 Analysis

The values for η of the first scan are plotted in fig. 37. An interval of $90\,\mu$m was selected around the charge sharing zone. A larger interval would include measurement points where the ADC-values are already affected by the aluminum strip.

There have been four different methods studied to get a function $\eta(x)$ respectively $x(\eta)$:

1. **Inverse function of a third order polynom (not pictured)**
   The function is too steep around $x = 0$ and too flat toward the edges.

2. **Point wise connection line (solid red line)**
   The method is highly prone to statistical fluctuations. The gradient of the function jumps at the data points leading to accumulation points. Further, as η may be not strictly increasing far away from the charge sharing zone, the inverse function is not defined.

3. **Function borrowed from the Fermi function (dash-dotted blue line)**

$$\eta(x) = \frac{a}{e^{-(x-\mu)/\varepsilon} + 1} + b \tag{11}$$
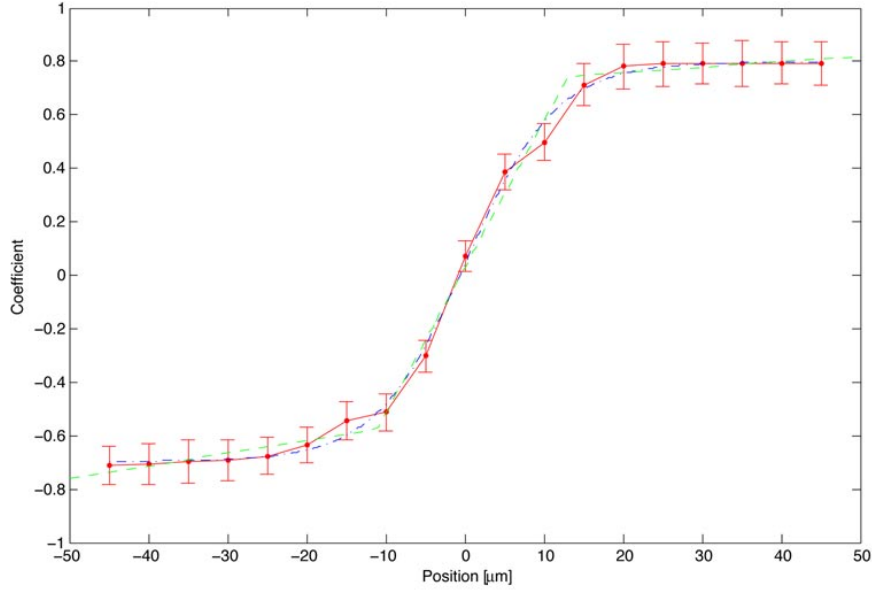
Figure 37: Plot of the measured η with the three used methods for $\eta(x)$; pointwise connection: solid red line, Fermi function: dash-dotted blue line, three linear sections: dashed green line. $x = 0$ is in the middle between the two strips.

This function has a desired smooth behavior, but is not surjective leading to problems in the reconstruction (complex reconstructed coordinates).

4. **Function consisting of three linear sections (dashed green line)**

$$\eta(x) = \min(\max(a_0 + a_1 x, b_0 + b_1 x), c_0 + c_1 x) \tag{12}$$

The function is bijective and the inverse does not create accumulation points. Besides statistical fluctuations are equalized by the regression. This method showed indeed the best results and was used for the reconstruction. There are the parameters received from the fit in tab. 6.

Table 6: Fitted parameters of 3-folded linear function

Parameter	offset (α_0)	slope (α_1) $[\mu m^{-1}]$
a	$(-5.2\pm0.7)\,10^{-1}$	$(4.7\pm2.2)\,10^{-3}$
b	$(2.9\pm0.2)\,10^{-2}$	$(5.4\pm0.3)\,10^{-2}$
c	$(7.2\pm0.8)\,10^{-1}$	$(1.9\pm2.5)\,10^{-3}$

In fig. 38 the reconstructed positions of all the events taken in the second scan are plotted versus their actual position. The plot shows that the reconstruction is quite good near $x = 0$ whereas it gets worse to the edges.
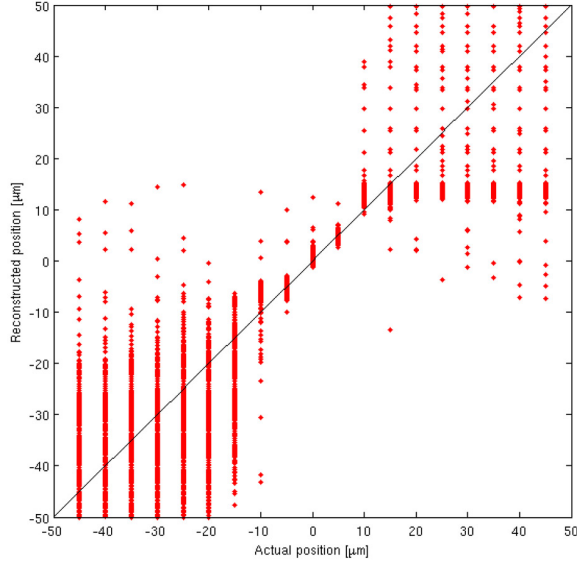
Figure 38: Plot of the reconstructed position for all the taken event versus the actual laser positions. The reconstruction leads to small variations near $x = 0$ caused by a larger slope of the used $\eta(x)$. Toward the edges the variation gets larger.

To estimate the spatial resolution of the sensor using this reconstruction method, two values were considered:

1.

$$r_1 = \sqrt{\frac{\sum_{i=1}^{N}(x_{r_i} - \overline{x_r})^2}{N}} \tag{13}$$

2.

$$r_2 = \sqrt{\frac{\sum_{i=1}^{N}(x_{r_i} - x_t)^2}{N}} \tag{14}$$

x_{r_i}: reconstructed position from the i$^{\text{th}}$ event
$\overline{x_r}$: mean of x_{r_i}
x_t: actual position of the laser beam

r_1 is the standard deviation of $\overline{x_r}$ making a statement about the variations of the reconstructed positions, but does not account for a possible bias between the mean reconstructed and actual position in contrast to r_2. Further $r_1 \leq r_2$ with equality only if $\overline{x_r} = x_t$.
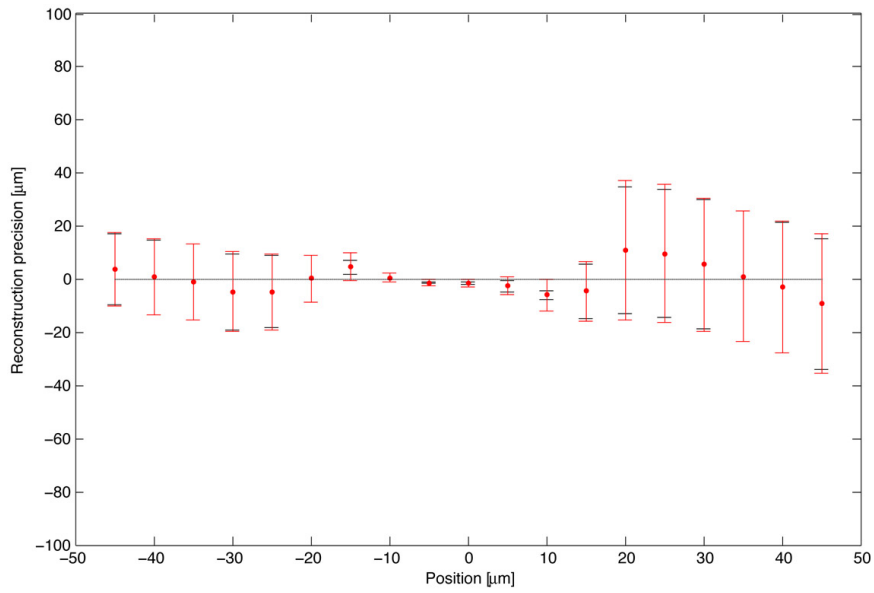
Figure 39: Plot of the reconstruction precision $\Delta x = \overline{x_r} - x_t$ with r_1 (black) and r_2 (red) as errorbars.
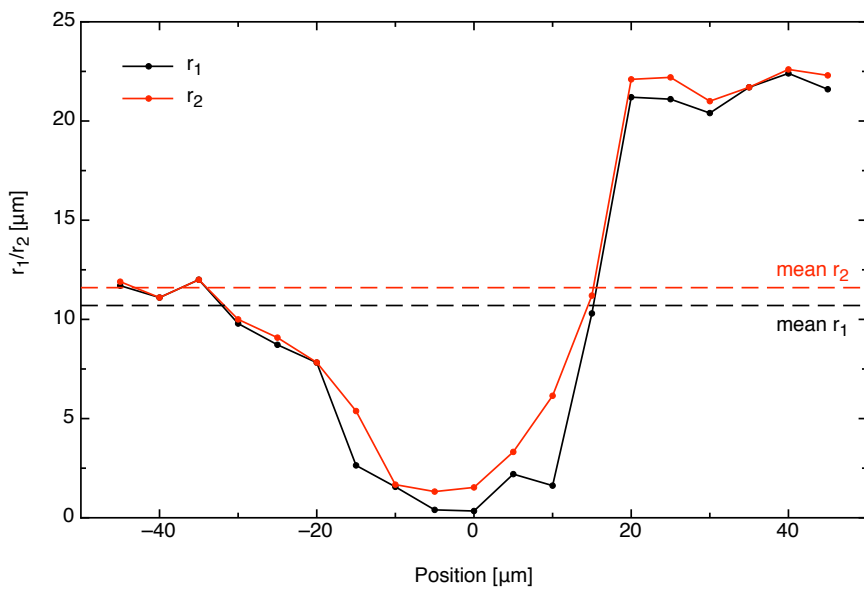
Figure 40: Plot of r_1 (black) and r_2 (red). Both values are small in the middle between the two strips while they are higher toward the edges. The resolution on the right side is worse due to the asymmetry of the ADC-values.

Fig. 39 shows for every position of the laser beam the *reconstruction precision* $\Delta x = \overline{x_r} - x_t$. Additionally the errorbars indicate r_1 (black) and r_2 (red). The spatial resolution under consideration of charge sharing is at every point much better than the binary resolution (max $r_1 = 21.7\,\mu$m, min $r_1 = 0.3\,\mu$m, mean $r_1 = 10.7\,\mu$m; max $r_2 = 22.5\,\mu$m, min $r_2 = 0.8\,\mu$m, mean $r_2 = 11.6\,\mu$m). Directly over the charge sharing zone the resolution is about 40 times better than the binary resolution and even on the edges the resolution is about twice as good (cf. fig. 40).

The resolution depends largely upon the shape of $\eta(x)$: The steeper the function is the better the resolution is for an equal variation on η is projected onto a smaller interval in x by $\eta(x)^{-1}$. Additionally the slope parameters of the outer sections have quite high relative errors (cf. tab. 6). As seen in fig. 37, $|d\eta/dx|$ is smaller toward positive than negative x resulting in a worse resolution. This difference in $|d\eta/dx|$ is caused by the asymmetry of the ADC-values: Fig. 36 shows that the ADC-values of channel 315 and 316 change more to the left of the charge sharing zone (x between -40 and $-15\,\mu$m) than to the right (x between $+15$ and $+40\,\mu$m). Therefore $|d\eta/dx|$ is larger on the left side and the variation of the reconstructed position is smaller at equal variations on η.

But it has to be remarked that the measurements have been done with a laser beam alignment such that the detector is just not saturated. Therefore the ADC values are higher than in the case of a minimal ionizing particle and out of this the signal-to-noise ratio is too high. As a consequence the variation on η is smaller than in the case of a minimum ionizing particle leading to an overestimated space resolution (or underestimated r_1 and r_2).

44

8 Broken bond

8.1 Problem

Soon after the installation of the half-modules in the TT station at LHC*b* it was found that a certain fraction of wire bonds connecting the Beetle-chip and the pitchadapter was broken. The fractures always appeared near the bond feet.

Due to lack of space the bond feet are arranged in four staggered rows. The problem appears in the innermost of these four bond rows. For example at the K-Hybrid of TT-module 111, all bonds of the innermost row of Beetle 0 and 1 are broken – most of them at the pitchadapter side.

So far there has no explanation been found and this topic is still under investigation.

## 8.2 Profile and crosstalk measurements

To get a first indication of the influence of broken bonds on the readout signal, a scan over a broken bond channel including its neighbors has been performed (last broken bond channel on Beetle 1: Channel 252). The ADC-values of the broken bond channel and the next higher and lower channel in fig. 41 are plotted, their rms-value in fig. 42.

As expected the broken bond channel features a lower signal and no indication of the laser beam. The neighboring channels show higher ADC-values when the laser beam hits the broken bond channel than in the common case. Despite the missing connection of the readout strip the bias voltage distribution is still working.

A further issue is that a small signal appears in the broken bond channel when one of the neighboring strips shows a high ADC-value. The reason is the electronic crosstalk in the Beetle chip. To test its asymmetry, the ADC-value of the broken bond channel is plotted against the summed ADC-value of its direct neighbors (cf. fig 43).

The crosstalk is highly symmetric as almost the whole variation on the broken bond channel is explained by the sum of the ADC-values on its neighboring channels. This is conflicting to the expectation (section 6.1): Broken bonds on Hybrid K109 are always even channels and one would expect a higher crosstalk from the succeeding channel than from the preceding channel.

But in general asymmetry between crosstalk from the succeeding and the preceding channel is smaller to even channels than to odd ones [16].
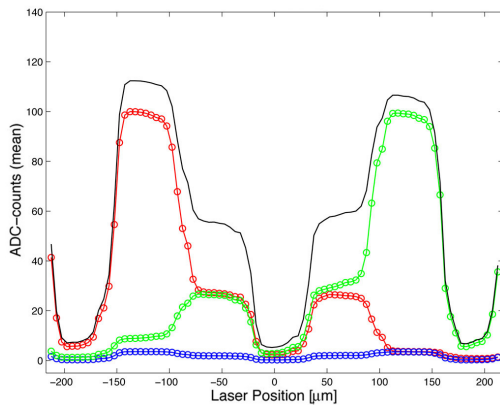
Figure 41: Signal on the broken bond channel (blue) depending on the laser beam position and its left (red) and right (green) neighbor. $x = 0$ refers to the center of the broken bond strip. On the broken bond channel there is no signal due to the laser beam but only variations due to electronic crosstalk.
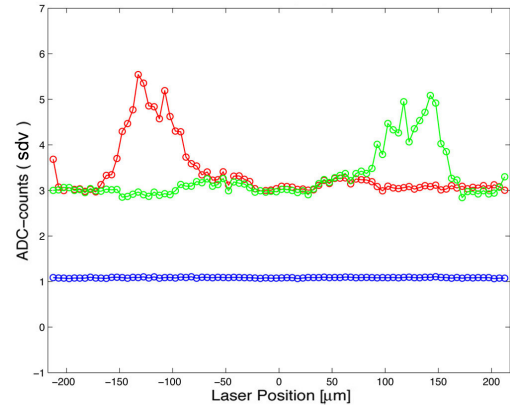
Figure 42: Noise on the broken bond channel (blue) and its left (red) and right (green) neighbor. Because of the missing connection to the readout strip the noise due to the capacitance of the strip falls away resulting in a lower total noise.
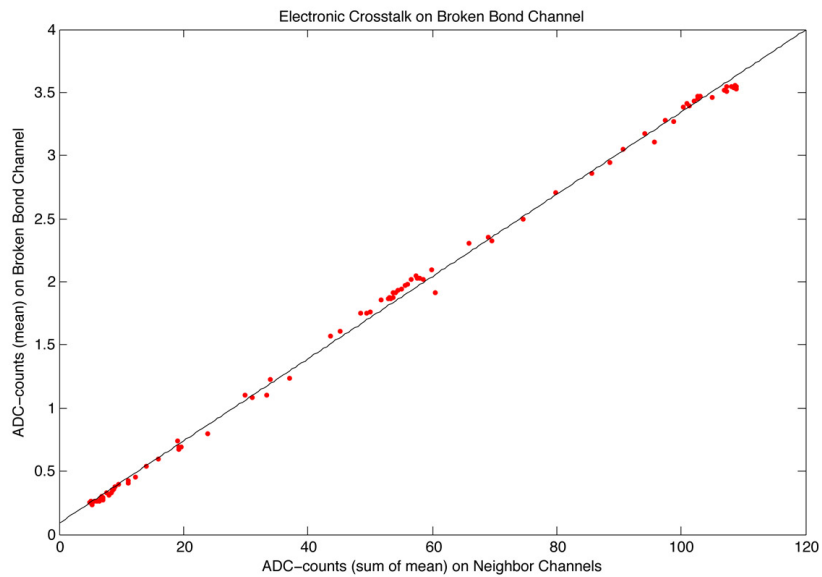
Figure 43: Plot of the ADC-value on the broken bond against the sum of the ADC-value on the direct neighbors. The linear regression shows a high correlation (99.9%) between the two values.

8.3 Spatial resolution

An interesting question about broken bonds is how the spatial resolution changes due to the unconnected readout strip. Again the charge sharing coefficient η_{BB} is considered, not between neighboring channels but between the neighbors $(i-1, i+1)$ of the broken bond channel (i):

$$\eta_{BB} = \frac{A_{i+1} - A_{i-1}}{A_{i+1} + A_{i-1}} \tag{15}$$

Figure 44: Plot of measured η_{BB} and fit functions (Pointwise connection: solid red line, Fermi function: dash-dotted blue line, three linear sectio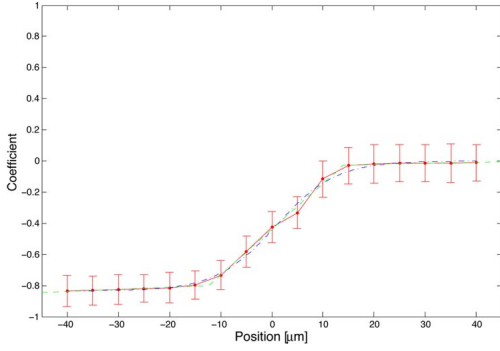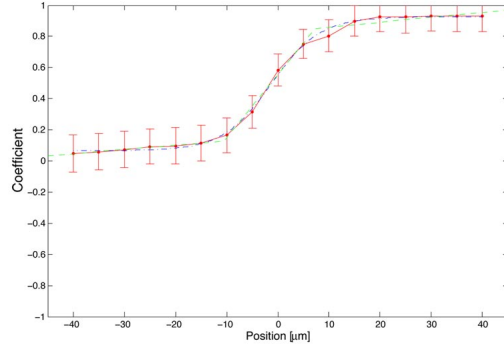ns: dashed green line) at the charge sharing zone between the broken bond and its left neighbor. $x = 0$ is in the middle between the two strips.

Figure 45: Plot of measured η_{BB} and fit functions (Pointwise connection: solid red line, Fermi function: dash-dotted blue line, three linear sections: dashed green line) at the charge sharing zone between the broken bond and its right neighbor. $x = 0$ is in the middle between the two strips.

Fig. 44 shows η_{BB} for the charge sharing between the broken bond channel and its left neighbor, fig. 45 between the broken bond channel and its right neighbor. The used method to construct a function $\eta_{BB}(x)$ is again to fit three linear sections to the data points (green line). Tab. 7 and 8 show the resulting parameters.

Table 7: Fitted parameters of 3-folded linear function (left)

Parameter	offset (α_0)	slope (α_1) $[\mu m^{-1}]$
a	$(-7.8\pm0.3)\,10^{-1}$	$(1.4\pm0.9)\,10^{-3}$
b	$(-4.4\pm0.1)\,10^{-1}$	$(2.9\pm0.1)\,10^{-2}$
c	$(-3.4\pm3.1)\,10^{-2}$	$(0.6\pm1.1)\,10^{-3}$

Table 8: Fitted parameters of 3-folded linear function (right)

Parameter	offset (α_0)	slope (α_1) [$\mu\mathrm{m}^{-1}$]
a	$(1.5\pm0.5)\,10^{-1}$	$(2.7\pm1.9)\,10^{-3}$
b	$(5.5\pm0.2)\,10^{-2}$	$(4.0\pm0.3)\,10^{-2}$
c	$(8.2\pm0.3)\,10^{-1}$	$(3.1\pm1.3)\,10^{-3}$
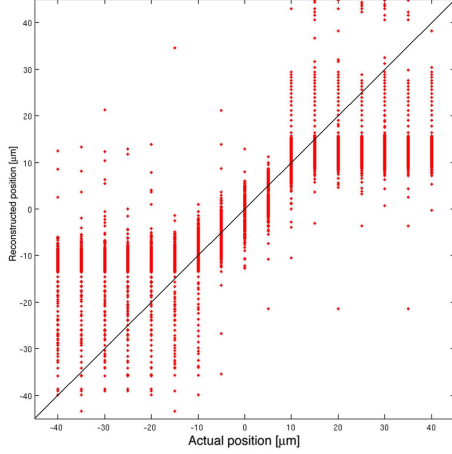
Figure 46: Plot of reconstructed positions against their actual positions for the left charge sharing

Figure 47: Plot of reconstructed positions against their actual positions for the right charge sharing

To estimate the spatial resolution a second scan has been done. In fig. 46 and 47 the reconstructed coordinates of all events against the actual laser coordinates are plotted (same procedure as in section 7.3).

For the left transition:

- $\max r_1 = 30.3\,\mu\mathrm{m}$, $\min r_1 = 3.0\,\mu\mathrm{m}$, $\mathrm{mean}\,r_1 = 19.4\,\mu\mathrm{m}$

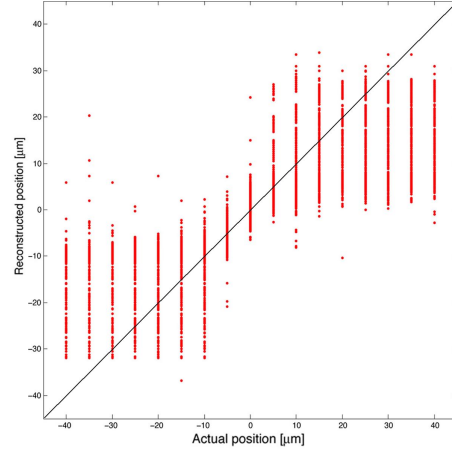- $\max r_2 = 30.3\,\mu\mathrm{m}$, $\min r_2 = 3.9\,\mu\mathrm{m}$, $\mathrm{mean}\,r_2 = 20.3\,\mu\mathrm{m}$

For the right transition:

- $\max r_1 = 25.7\,\mu\mathrm{m}$, $\min r_1 = 3.6\,\mu\mathrm{m}$, $\mathrm{mean}\,r_1 = 17.8\,\mu\mathrm{m}$

- $\max r_2 = 26.8\,\mu\mathrm{m}$, $\min r_2 = 4.0\,\mu\mathrm{m}$, $\mathrm{mean}\,r_2 = 18.8\,\mu\mathrm{m}$

Discussion In comparison to the case of normal strips, the resolution does not suffer much at the edges of the charge sharing zone from a common strip but in the center the resolution is worse. This would implicate that even in case of broken bonds an acceptable spatial resolution can be achieved if a suitable algorithm is used.

The reason is that due to the consideration of a strip not involved in the charge sharing the values of η_{BB} can only vary in the intervals $[-1, 0]$ respectively $[0, 1]$. This leads to a smaller slope of the central linear section (reduced by about a factor 2) and therefore to a higher variation of the reconstructed coordinates.

Fig. 48 and 49 show again the reconstruction precision $\overline{x_r} - x_t$ with r_1 and r_2 as errobars. The missing of asymmetry prevents large differences in the slope of the two outer sections. Therefore the variations in the reconstructed positions are not as different as in the common case (cf. fig. 50 and 51).
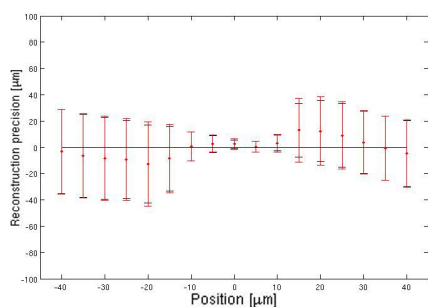
Figure 48: Plot of $x_r - x_t$ with r_1 (black) and r_2 (red) as errorbars for the left charge sharing

Figure 49: Plot of $x_r - x_t$ with r_1 (black) and r_2 (red) as errorbars for the right charge sharing

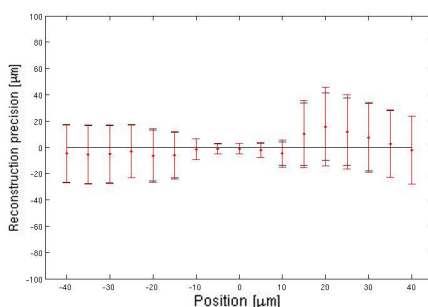There has been also a reconstruction performed over both charge sharing zones togehter. In this case a five folded linear function was used to describe $\eta_{BB}(x)$ and the readout strip of the broken bond was masked. But this method led to a worse resolution than a separated consideration.
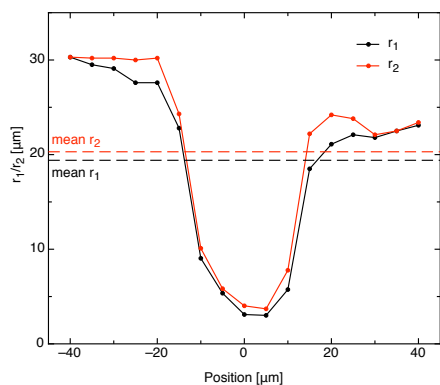
Figure 50: Plot of r_1 (black) and r_2 (red) for the left charge sharing.
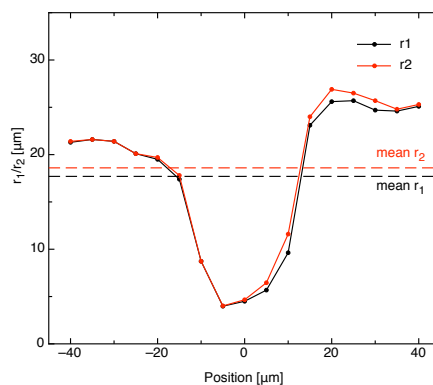
Figure 51: Plot of r_1 (black) and r_2 (red) for the right charge sharing.

References

[1] A. A. Alves et al. [LHC*b* Collaboration], *The LHC*b *Detector at the LHC*, JINST 3, 2008.

[2] C. Amsler, *Kern- und Teilchenphysik*, 1. Auflage, vdf Hochschulverlag AG, ETH Zürich, 2007 (German).

[3] C. Bauer et al., *Grounding, Shielding and Power Distribution for the LHC*b *Silicon Tracking*, CERN, LHC*b*-Note 2004-101, 2005.

[4] J. Buytaert, *Beetle1.3 validation for VELO* (Presentation), http://www.kip.uni-heidelberg.de/lhcb/Meetings/Meeting200404/Beetle_user_velo.pdf (Access: 6 October 2009).

[5] J. Christiansen et al. *TTCrx Reference Manual*, Version 3.11, CERN, 2005.

[6] J. Gassner et al., *Measurements of Prototype Ladders for the TT station with a Laser*, University of Zurich, LHC*b*-Note 2004-102, 2005.

[7] Guido Häfeli, *Contribution to the development of the acquisition electronics for the LHC*b *experiment*, PhD thesis, EPFL, 2004.

[8] N. Harnew, *B-Physics Prospects with the LHC*b *Experiment*, Physics of Atomic Nuclei (2008), Vol. 71, No. 4, 588 - 604.

[9] Ch. Kittel, *Einführung in die Festkörperphysik*, 14. Auflage, Oldenbourg, 2006 (German).

[10] K Kleinknecht, *Detectors for Particle Radiation*, 2nd edition, Cambridge University Press, 1998.

[11] K. Kleinknecht, *Uncovering CP-Violation, Experimental Clarification in the Neutral K Meson and B Meson Systems*, Springer-Verlag, Berlin, Heidelberg, New York, 2003.

[12] G. Landolt, *Setting up an LHC*b *TT-Detector Test Stand*, Bachelor thesis, University of Zurich, 2009.

[13] F. Lehner, *The LHC*b *Silicon Tracker*, CERN, LHC*b*-Note 2005-077, 2004.

[14] S. Löchner, M. Schmelling, *The Beetle Reference Manual – chip version 1.3, 1.4 and 1.5*, Max-Planck-Institute for Nuclear Physics, document version 1.73, 2006.

[15] S. Löchner, *Development, Optimisation and Characterisation of a Radiation Hard Mixed-Signal Readout Chip for LHCb*b, PhD thesis, Ruperto-Carola University of Heidelberg, 2006.

[16] S. Löchner, *Lab Measurements with the Beetle 1.3 (Update)*, CERN, 2004, http://www.kip.uni-heidelberg.de/lhcb/Publications/LHCb/LHCb_Feb2004.pdf (Access: 21 September 2009).

[17] H. Spieler, *Semiconductor Detector Systems*, 1st edition, Oxford University Press, 2005.

[18] O. Steinkamp, *Design and Production of Detector Modules for the LHCb Silicon Tracker*, Nuc. Instr. Meth. A (2007), 579, 736 - 741.

[19] A. Vollhardt, *An Optical Readout System for the LHCb Silicon Tracker*, PhD thesis, University of Zurich, 2005.

[20] LHC*b*-group, University of Zurich, http://lhcb.physik.uzh.ch/.

[21] *Properties of CMS-OB2-SSSD sensor type*, http://lhcb.physik.uzh.ch/tt/sensorprob/S9153-04B.pdf (Access: 10 September 2009).

[22] Analog Devices, *Datasheet Thermoelectric Cooler Controller ADN8830*, http://www.analog.com/static/imported-files/data_sheets/ADN8830.pdf (Access: 7 October 2009).

[23] Emis GmbH, *Technisches Handbuch Schrittmotorsteuerkarte SMC800/SMC1500*, (German), http://www.emisgmbh.de/smc800exe.htm (Access: 14 April 2009).

[24] JDS Uniphase, *Product Bulletin Manual Variable Optical Attenuators (VA4 Series)*, http://www.datasheetarchive.com/VA4-datasheet.html (Access: 25 May 2009).

[25] QPhotonics, *Datasheet QFLD-1060-30S-AR*, http://www.qphotonics.com/product_image.php?imageid=558 (Access: 25 May 2009).

[26] Tandon Motors Pvt. LTD (India), *Datenblatt Schrittmotor Tandon KP4M2-203*, http://www.cybertux.nl/elektronica/datasheets/Stappenmotoren/Conrad%20967645-da-02-de-Schrittmotor.pdf (Access: 14 September 2009).

[27] Terahertz Technologies Inc., *Specifications TIA-950 O/E Converter*, http://www.metrotek.com/tia950datasheetweb.pdf (Access: 16 September 2009).

[28] Virginia Semiconductor Inc., *Optical Properties of Silicon*, http://www.virginiasemi.com/pdf/Optical%20Properties%20of%20Silicon71502.pdf (Access: 19 September 2009).

A The Test Stand Manual

This is an updated version of the manual describing how to operate the test stand (status: November 7, 2009).
The sections about front-end electronics, trigger sending and data acquisition are taken over from [12] with only slight modifications.

A.1 How To Control Front-End Electronics
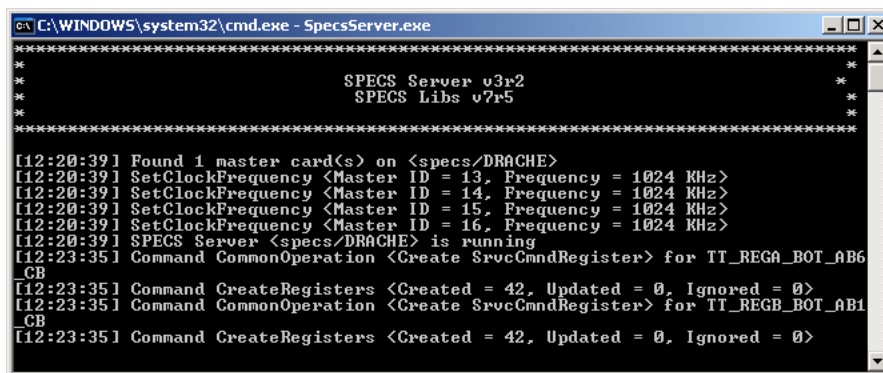
- Before starting the front-end electronics, make sure that the cooling system is running (how to control it is described in A.6).

- Make sure, that the DIM name server (DNS) is running on pc *lama*'s *Linux*-partition: Type in a console

  ```
  $ ps aux | grep /app/lhcb/pvss/PVSS_tfc/ ...
  fwComponents_20050810/bin/dns
  ```

  DNS is running if the corresponding process is prompted.

  The PVSS-project for controlling the Odin must not be running.

- Log into the *WINDOWS*-booted pc *DRACHE* as *Institut*.

Figure 52: SPECS-server output after successful subscription of the Control Board hardware type

- Start the SPECS-server: Open a *WINDOWS* command prompt. Go to the project directory:

  ```
  : cd C:\ETM\PVSS2\3.6\TEST_STAND1\bin
  ```

  Set the environment variable *DIM_DNS_NODE*:

```
: set DIM_DNS_NODE=lama.physik.uzh.ch
```

Start the SPECS-server:

```
: SpecsServer.exe
```

Don't close the window.

- Start the PVSS Administration in the *WINDOWS* Start menu.

- Select the project *TEST_STAND1*, hit the refresh button and then the green traffic light to start up the project. Wait until the whole project is loaded.
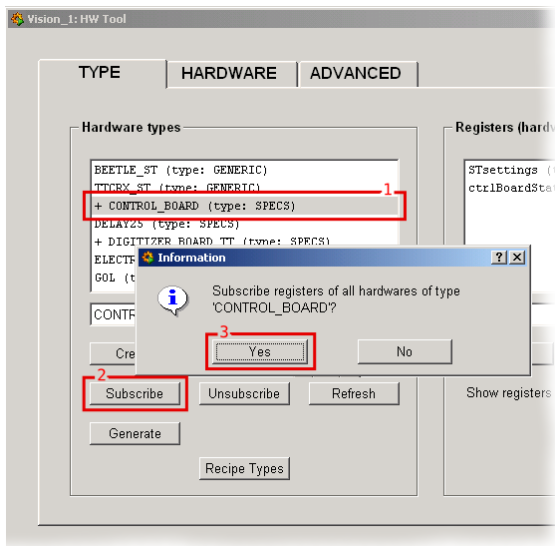
Figure 53: Subscription at the SpecsServer of hardware-types
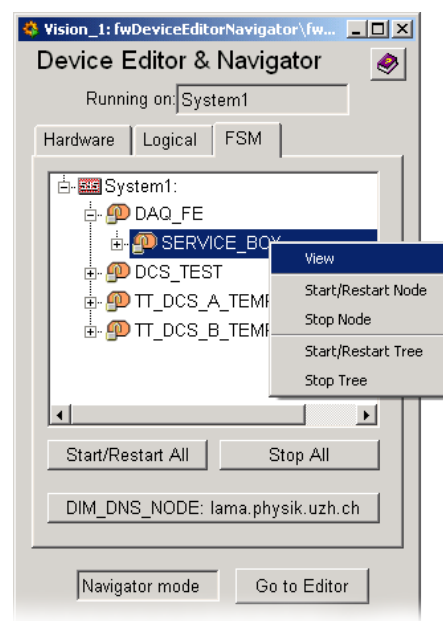
Figure 54: Device Editor & Navigator. Control unit objects marked with a lock, devices labelled with a yellow oval.

- Go to the panel called *HW Tool* and subscribe each hardware-type:

  1. select each one of the items listed under the tab *TYPE*

  2. hit `Subscribe`

  3. accept the prompts.

  If the subscription was successful one can see in the output in the SPECS-server window (fig. 52). Otherwise restart the server and try again. See fig. 53.

- Go to the panel *Device Editor & Navigator*. Change to the tab *FSM* and ensure that you are in the `Navigator mode`. Perform `Start/Restart All`. Wait until the prompt disappears. See fig. 54.

- Initialize SPECS and power partitions: Right-click on `DCS_TEST`, in the appearing menu choose *View*.

  A window will open displaying all the sub-systems and their states. In this case the object is `DCS_BOX`. Take over control by clicking on the lock-sign and then pushing `Take`, the color of the drop-down menu displaying `NOT_READY` should change to yellow. Click on the `NOT_READY` and select from the drop-down menu `SWITCH_ON`. To configure send the recipe `PHYSICS` in the appearing window. The drop-down menu should change to green ground and the state `READY`. Further the red LED mounted on the box is on.

- Initialize front-end electronics: In the *Device Editor & Navigator* window right-click on the item `DAQ_FE`, choose *View*, take over the control. Click on the `NOT_READY` and select from the drop-down menu `Configure`. Use again the recipe `PHYSICS`. Because this is the wrong recipe for the ladders, the drop-down menu will turn into red and display `ERROR`. To correct this select from the drop-down menu `Recover`. The devices in error will go back to `NOT_READY` as well as the drop-down menu. Now select `Configure` again, but this time with the recipe `TEST|VFS400_NOTP`. The drop-down menu will show on blue ground `READY`.

- Start temperature readout: In the *Device Editor & Navigator* window right-click on `TT_DCS_B_TEMP_BOT_AB1`, then choose *View*. After setting *READY* `TT_AB1_HYBR_TEMP_P5X2` and `TT_TEMP_SBAB1`[9] the temperatures of the Hybrid- and Control Board-sensors are readout.

  View the temperature curves: If not yet done start the *Trending Editor & Navigator* (look for `fwTrending` in the PVSS console). Ensure that it's in *Navigator mode*. Click on *Manage Plots/Pages*. Right-click on `System1:HYBR_TEMPS_3DB` to see the temperature plots (`CTRL`-`4` and -`8` allows zooming out in the x- and y-axis). Left-click allows configuration of the plot.

- A switch off has to be done by clicking on every drop-down menu displaying `READY` and choosing in the menu `Reset` or `Switch_OFF`. Note that objects can propagate commands to their sub-systems.

---

[9]Due to a non-relevant programming error this device will change its state to *ERROR*.

A.2 How To Send Triggers

- Login in the Linux-boot of *lama* as *lhcb*.

- Check whether DNS is running[10]:

  ```
  $ ps aux|grep dns
  ```

  and look for `/app/lhcb/pvss/PVSS_tfc/` ...
  `fwComponents_20050810/bin/dns`.
  If not start it:

  ```
  $ /app/lhcb/pvss/PVSS_tfc/fwComponents_20050810/. ..
  bin/dns
  ```

  Important: If `ps aux|grep dns` delivers more than two processes, then the
  PVSS-project for Odin might be running. *The Odin-PVSS-project has to be shut
  down properly.*

- Check if sticky bit of `/tmp` is cleared:

  ```
  $ ls -ld /tmp
  ```

  If not clear it (as root):

  ```
  # chmod -t /tmp
  ```

- Start lock manager:

  ```
  $ source /app/lhcb/pvss/PVSS_tfc/setup
  ```

- Start Odin: Log in:

  ```
  $ ssh tfc@odinv100
  ```

  Password: `amex`
  Execute:

  ```
  $ start_TFC
  ```

  Don't close the shell.

- Start PVSS-project: In a new console type:

  ```
  $ startConsole
  ```

  Click on the green traffic light to start the project `TFC_LC`

---

[10]Use in general *XTerm* instead of normal consoles preventing memory overflows!
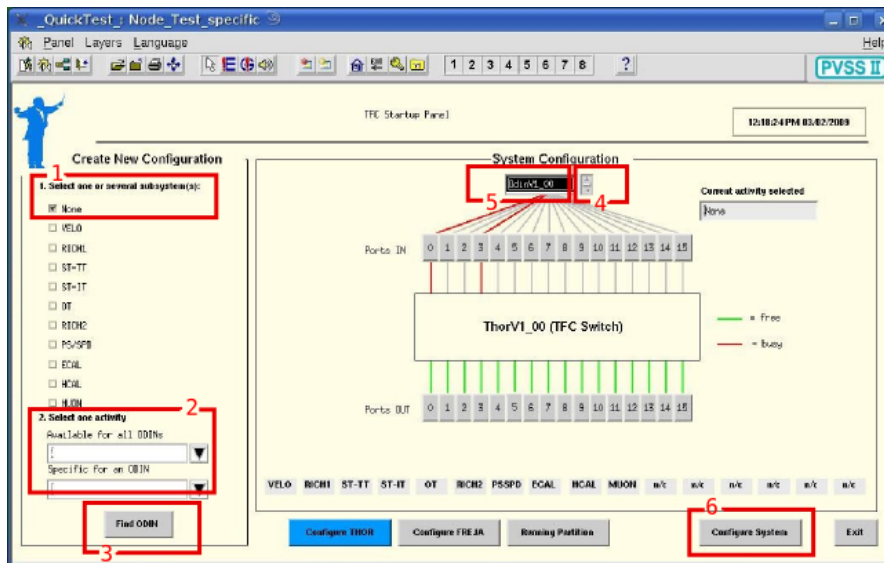
Figure 55: TFC Startup Panel

- Go to the *Graphic Editor*, click on *Panel → Open* and select TFC_LC/panels/
  TFC_top.pnl. Start the panel by clicking *Panel → Save & View*.

The following steps are visualized in fig. 55.

- **1.** *Select one or several subsystem(s)* tick None.

- **2.** *Select one activity* choose None for *Available for all ODINs*.

- **3.** Click [Find ODIN]. Wait until in *System Configuration* Port 0 is highlighted
    red.

- **4.** Cycle through the prompt displaying OdinDef and pick OdinV1_00.

- **5.** Click into the prompt. The Port 3 will highlight red.

- **6.** Click on [Configure System].

The window *TFC Local Run Control* should have opened. The numbers in the text refer
to fig. 56.

- **1a/b.** Verify that the states of Partition_OdinV1_00 and OdinV1_00 are
    both RUN_NOT_READY on orange ground. If this is not the case one has to
    perform a restart either of the project or of the entire PVSS environment.

- **2.** In the section *Initialization* click on [Subscribe Cnts] and [Counter Reset].

- **3.** One can choose the desired triggers under section *L0 trigger*, e.g. *Periodic*

trigger A.

- **4.** The configuration of the trigger can be done by clicking on `ODIN not ready` in the *Configuration* section.

  5. Configuration concerning the trigger frequency, offset and length or delay respectively for periodic and calibration trigger can be set in the *Periodic/calibration trigger SM* section. `Current` loads the current data (right column), `Default` loads the default data, `Apply` applies the new values (left column).

  6. `Apply (all)` writes the desired configuration. (`Default all` can be useful after a loss of standard configuration.)

- **1a.** In order to start triggering click on the upper orange button `RUN_NOT_READY`, then on `GET_READY` and finally on `START_RUN`.

  7. The L0 Trigger numbers should now count up.

- To avoid problems restoring the correct latency after the front end electronics have been off, it is advisable to make a *Soft Reset* by clicking on the `Soft Reset` in the window `Partition_OdinV1_00`. The Odin changes to the state described in **1a/b.**, but keeps the settings. Then perform a reset of the L0 Trigger by clicking in the window `ODIN_settings` on `Single shots`. A window appears with all the possible single shots. Click on `Shoot` next to `L0 Electronics Reset`.

A.3 How To Switch on the Laser

- Make sure that the flexes from Odin via NIM-crate into the test box are laid correctly (Connection `P1-R` on the Odin).

- Switch on the power supply next to the test box.

A.4 How To Control the High Voltage

- Open the program `St225.vi` or `St226.vi`[11] in the folder `HV-Steuerung` on the `Institut` account at `DRACHE`.

- Make sure that the selected port in the program (usually `COM3` or `COM4`) corresponds to the connection.

---

[11] `St225.vi` is to steer NHQ-225-modules whereas `St226.vi` is for NHQ-226-moduels
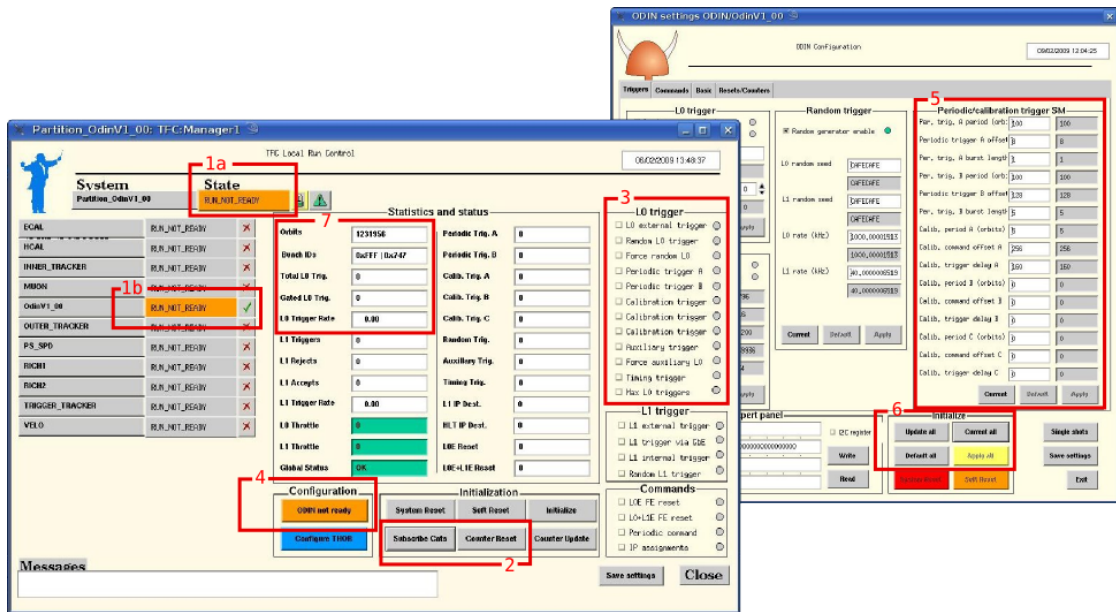
Figure 56: left: TFC Local Run Control, right: Odin Configuration

- Start the VI (Press the white arrow button in the prompt, turns to black). If the status display is green, the module is ready.

- If the status display is red, check the rocker switches Contr. (should be on DAC) and HV (should be on ON) at the modul.

- To change the target voltages, the ramp speeds or the delay time, put the designated value into the according box by keyboard and confirm it by clicking on to the control panel.

- To start changing the applied voltage to the target value hit CHANGE. While changing the applied voltage the status display is yellow.

- To bring the applied voltage immediately to 0 V, hit the switch Emer..

- To avoid any accidental changing of the settings, hit the switch Block. A red light will appear.

> Never turn high voltage on while the box is open!
> It immediately leads to breakdown current.

Figure 57: LabView panels; left: HV control, top right: step motor control, down right: Polystat control
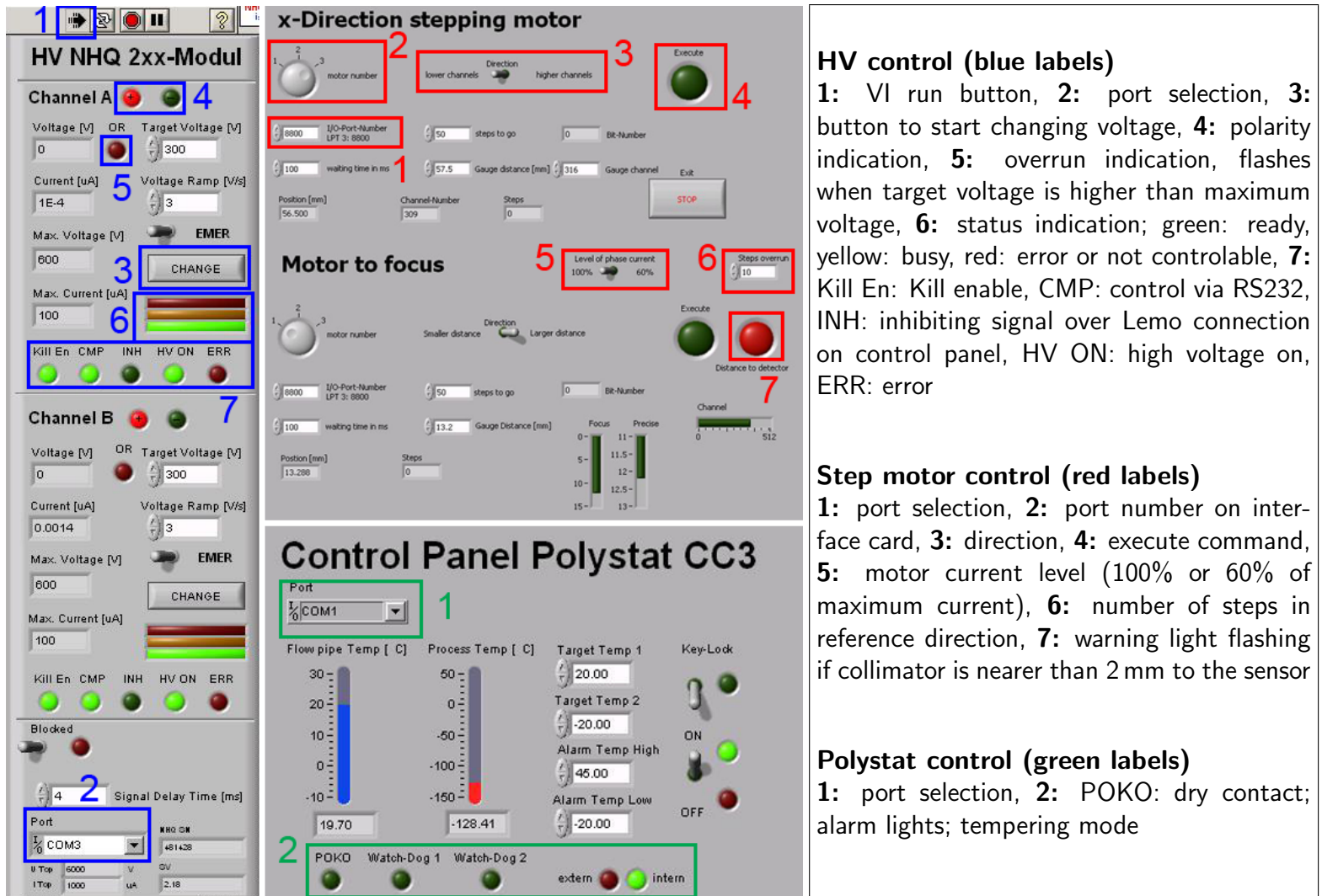
HV control (blue labels)
1: VI run button, **2:** port selection, **3:** button to start changing voltage, **4:** polarity indication, **5:** overrun indication, flashes when target voltage is higher than maximum voltage, **6:** status indication; green: ready, yellow: busy, red: error or not controlable, **7:** Kill En: Kill enable, CMP: control via RS232, INH: inhibiting signal over Lemo connection on control panel, HV ON: high voltage on, ERR: error

Step motor control (red labels)
1: port selection, **2:** port number on interface card, **3:** direction, **4:** execute command, **5:** motor current level (100% or 60% of maximum current), **6:** number of steps in reference direction, **7:** warning light flashing if collimator is nearer than 2 mm to the sensor

Polystat control (green labels)
1: port selection, **2:** POKO: dry contact; alarm lights; tempering mode

A.5 How To Control the Stepping Motors

- Check power supply of the SMC800 interface.

- Open the program `Step_control.vi` in the folder `Step_control` on the `Institut` account at `DRACHE`.

- Make sure that the selected port in the program (usually `LPT3`) corresponds to the connection[12].

- Start VI.

- Be sure that the chosen motor numbers correspond to the actual connection.

- Select the number of steps and the direction.

- Hit `Execute`. Flashing green means the system waits until the previous running commands are finished.

- Before closing the program move back to the zero point. After restarting the program the actual point will be set to be zero.

A.6 How To Control the Cooling Device

- Open the program `Polystat_CC3.vi` in the folder `Polystat` on the `Institut` account at `DRACHE`.

- Make sure that the selected port in the program (usually `COM1`) corresponds to the connection.

- Start the VI.

- Put the rocker switch to `ON`.

- To change target or alarm temperatures, write down the desired value into the corresponding box.

- To avoid manipulations directly on the operator device, switch on the `Key lock`.

A.7 How To Start Data Aquisition

- You must be logged in the Linux-boot of *lama*.

- Connect to the TELL1's credit card pc:

---

[12]The hexadecimal code for `LPT3` is 0h8800.

```
$ ssh cc@ccpc18
Password: amex
```

- Start aquisition:

```
$ daq_tell1 ST5.v26_TTTELL01_labUZH.cfg
```

- Log into *Kamel*. Open a root-console. Change to the Event Builder directory:

```
# cd /home/hep/lhcb/Desktop/Gabriel/ ...
ebuild/writeEventsToBinary
```

- Write `<number>` events to binary file `<file>`:

```
# ./writeEventsToBinary <file> <number>
```

(Binary files can be opened with `hexdump <file> | less`. The data is built out of the following elements: (magic pattern) (bank size) (version/type) (source ID). The magic pattern is in hex: `cbcb`.).

- Send desired triggers with Odin.

A.7.1 How To Open Data in ROOT

- Log into a machine on which the Gaudi anaylsis software is installed in the user's home directory and open a z-Shell. Append the following lines to the `~/.zshrc`-file.

```
# Environment for ROOT
export ROOTSYS=${CERN}/root ;
export PATH=${PATH}:${ROOTSYS}/bin ;
export LD_LIBRARY_PATH=${LD_LIBRARY_PATH}:
${ROOTSYS}/lib

# Environment for LHCb software
export MYSITEROOT=/app/lhcb/sw-slc4
export CMTCONFIG=slc4_ia32_gcc34
export CMTPATH=$HOME/cmtuser
export PATH=$MYSITEROOT/local/gcc-3.4.6/bin:
$MYSITEROOT/local/binutils-2.15.92.0.2/bin:
$MYSITEROOT/scripts:$PATH
export LD_LIBRARY_PATH=$MYSITEROOT/local/gcc-3.4.6
/lib:$MYSITEROOT/local/binutils- ...
2.15.92.0.2/lib:$MYSITEROOT
```

```
/lib:$LD_LIBRARY_PATH
. $MYSITEROOT/LbLogin.sh
```

- Make sure the folder `TTAnalysis.v7r1p1` is in the home directory (If not, copy it from `/home/hep/tobin`)

- Execute the following in a z-Shell:

```
$ SetupProject Vetra v7r1p1
$ cd TTAnalysis.v7r1p1
```

- Copy binary file to the current machine. Generate `.root`-file:

```
$ ./GetData <file>
```

The names of the `.root`-files are displayed on the last line of the output.

- To open the histogram-file with *ROOT*:

```
$ root <file.root>
```

- To convert the n-tuples-file to an ASCII-file with *ROOT*:
  Open *ROOT*:

```
$ root
```

Compile the converting program:

```
$ .L plotTuple2.C+
```

Select the desired readout channels:

```
$ plotTuple2("<file.root>", ...
<chnl #>, <# of chnls on each side>)
```

B Step Motor Details

The two used step motors are bipolar step motors. Tab. 9 shows their specifications.

Table 9: Technical data of step motors (Tandon KP4M2-203) [26]

Parameter	
Number of phases	2
Resistance per phase	37.5 Ω
Max. current per phase	0.15 A
Voltage	12 V
Angle per step	1.8°
Weight	270 g

Their connection to the used step motor interface card SMC800 is shown in fig. 58. The interface is able to control a maximal number of three motors. The structure of the bytes sent to the interface card triggering the steps is indicated in tab. 10. Tests have shown that the run stability is increased if the phase currents are not turned on and off but their direction is switched. Further it was found that an operation of the motors with only 60% of the maximal phase current allows a smoother motion but does not decrease run stability.

A half step mode has not been implemented as the minimal laser profile is well above the resolution of a half step in x-direction. Also an acceleration mode for long distances has not yet been integrated in the control software which would be supported by the interface card.

The used byte order for the two step motors is indicated in tab. 11.

The adjustment of the phase currents is performed by a trim-potentiometer per motor output on the interface card (cf. fig. 59). The voltage between trim-potentiometer and ground (negative terminal of current supply) $V_{tp,g}$ has to be measured and used to calculate the phase current I_{ph} by formula (16) [23], [26].

$$I_{ph}\,[\text{A}] = 0.084 \cdot V_{tp,g}\,[\text{V}] \tag{16}$$

Table 10: Byte structure for step motor interface SMC800 [23]

Bit number	8 & 7	6	5 & 4	3	2 & 1
Indication	motor no.	Dir. I_{ph} B	Lev. I_{ph} B	Dir. I_{ph} A	Lev. I_{ph} A
Meaning	00: x-axis		11: 0%		11: 0%
	01: y-axis		10: 20%		10: 20%
	10: z-axis		01: 60%		01: 60%
			00: 100%		00: 100%
			of max. current		of max. current

Table 11: Byte sequences used at the test stand

Motor	Byte sequence*				Lev. I_{ph}
x-axis	00100000	00100100	00000100	00000000	100%
	00101001	00101101	00001101	00001001	60%
z-axis	10100000	10100100	10000100	10000000	100%
	10101001	10101101	00001101	10001001	60%

*) Running through the sequence from left to right performs one rotating direction and from right to left the other.
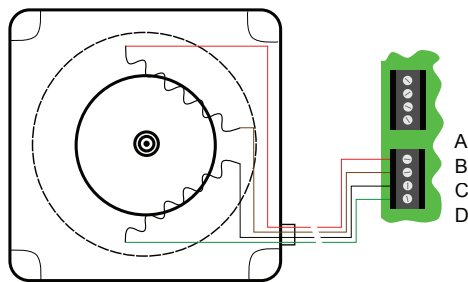
Figure 58: Scheme of the connection between a step motor and the terminals on the interface card including their notation.
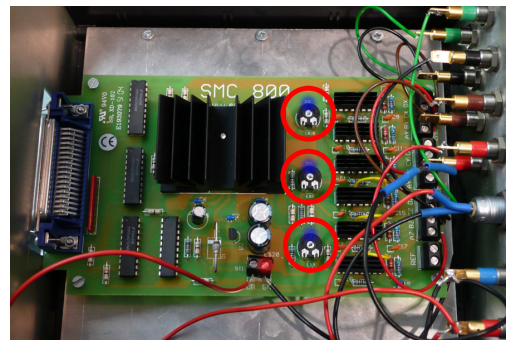
Figure 59: Picture of interface card SMC800 mounted inside its box. The red circles mark the three trim-potentiometers and the blue and red dots the measurement points for $V_{tp,g}$.

C Programs

C.1 Data Processing

plotTuple2.C The root-program `plotTuple2.C`, written by Mark Tobin, stores the ADC-values of a range of readout channels from a root-file into a tab-separated ASCII-file.

Input:	root-file <name>-ntuple.root
Parameters:	number of central channel, number of strips to the right and left
Output:	ASCII-file <name>-ntuple.root.dat
Command:	`plotTuple2(‘‘name>-ntuple.root’’, # of central channel, # of strips to the right and left)`
Code:	

Listing 1: plotTuple2.C: Program to convert root- to ASCII-File

```
1  #include "TTree.h"
2  #include "TFile.h"
3  #include "TProfile.h"
4  #include <vector>
5  #include <iostream>
6  #include <fstream>
7  #include <string>
8  void plotTuple2(const char* filename="/home/hep/tobin/...
9  data/2009.06.23/histo_190609_03-ntuples.root", ...
10 const int strip=345, const int width=3) {
11
12    ofstream myfile;
13    std::string fileout = filename;
14    fileout += ".dat";
15    myfile.open (fileout.c_str());
16
17    std::cout << "Dumping to " << fileout << std::endl;
18    TFile* file = new TFile(filename);
19    TTree* T = (TTree*)gDirectory-> ...
20    Get("TTDumpADCs/rawADCs");
21    std::vector<float> adcs(3072,0.);
22    T->SetBranchAddress("SourceID10",&adcs[0]);
23    int n = T->GetEntries();
24
```

```
25    // Writing a line
26    for(int i=0; i<n; i++) {
27        T->GetEntry(i);
28        for(int j=-width; j<width+1; j++) {
29            myfile << adcs[strip+j] << "\t";
30        }
31        myfile <<  "\n";
32    }
33    myfile.close();
34    file->Close();
35
36 };
```

GetData.m The MATLAB-program `GetData.m` calculates from a tab-separated ASCII-file containing the ADC-value per event of some channels their mean- and rms-value. Some auxiliary measurements without any laser signal are necessary to perform pedestal subtraction.

Input:	.dat-files as pedestal data and raw data
Parameters:	none
Output:	mean.dat, std.dat
Command:	GetData
Code:	

Listing 2: GetData.m: Program to gain signal and noise ADC-values per strip

```
1  %%% GetData
2
3  clear
4
5  %%% Serie number of measurement
6  serieNumber = 1;
7  centralStrip = 2785;
8  StripsOnSide = 2;
9
10 %%% Pedestal
11 % Signatur of pedestal measurement (NoSignal)
12 ped_praeambel = 'NS';
13 % Number of measurements for pedestal calculation
14 n_o_NS = 6;
15 ped = [];
```

```matlab
16
17 for i=0:n_o_NS-1;
18     data = load(['histo_',ped_praeambel, ...
19     sprintf('%d',serieNumber*1000+i),'-ntuples.root.dat']);
20
21     ped = [ped; data];
22 end
23
24 ped_dat = mean(ped);
25 ped_sig = std(ped);
26 %
27
28 %%% Signal and Noise
29 % Signatur of measurement (e.g. PulseScan)
30 praeambel = 'PS';
31 % Number of raw data measurements
32 n_o_D = 26;
33
34 mes = [];
35
36 for i=0:n_o_D-1;
37     data = load(['histo_',praeambel,sprintf(...
38     '%d',serieNumber*100000+i),'-ntuples.root.dat']);
39
40     mes = [mes;data];
41 end
42
43 dat = mean(mes) - meshgrid(ped_dat,0:n_o_D-1);
44 sdv = std(mes);
45
46 si = size(dat);
47 measurement=0:si(1)-1;
48 strip=-StripsOnSide:StripsOnSide + centralStrip;
49 measurementMesh = meshgrid(measurement,strip);
50 stripMesh = meshgrid(strip,measurement);
51
52 %%% Plotting of dat
53 screenSize = get(0,'ScreenSize');
54 figure('Position',[1 1 screenSize(3)/1.6 screenSize(4)/2])
55 surf(measurementMesh',stripMesh,dat)
```

```
56  view ( 0 , 0 )
57  hold  on
58
59  %%% Saving of data files
60  save ( [ 'mean' , sprintf ( '%d' , serieNumber ) , '.dat' ] , ...
61  'dat' , '−ascii' , '−tabs' )
62  save ( [ 'std' , sprintf ( '%d' , serieNumber ) , '.dat' ] , ...
63  'sdv' , '−ascii' , '−tabs' )
```

C.2 Profile reconstruction

ProReco.m   The MATLAB-program `ProReco.m` calculates with use of given error functions from a signal and an rms n-tuple representing the scan profile over a beam-covering object the corresponding beam profile.

Input:	signal and rms n-tuples, coordinate n-tuple, error functions
Parameters:	none
Output:	three figures
Command:	`ProReco`
Code:	

Listing 3: ProReco.m: Program to reconstruct beam profile

```
1   %%% ProReco
2
3   save_format  =  'pdf';
4   measurement  =  2;
5   dat  =  load ( [ 'mean' , sprintf ( '%d' , measurement ) , '.dat' ] );
6   sdv  =  load ( [ 'std' , sprintf ( '%d' , measurement ) , '.dat' ] );
7   coo  =  load ( [ 'coo' , sprintf ( '%d' , measurement ) , '.dat' ] );
8   si   =  size ( dat );
9
10  % Simulated = 1, Calculated = 0;
11  sim  =  0;
12
13  % Region of Interest in array number of 'coo'
14  RegOfInter  =  [ 1  14 ];
15  dat  =  dat ( RegOfInter ( 1 ) : RegOfInter ( 2 ) );
16  sdv  =  sdv ( RegOfInter ( 1 ) : RegOfInter ( 2 ) );
17  coo  =  coo ( RegOfInter ( 1 ) : RegOfInter ( 2 ) );
```

```matlab
18  extrema = [min(coo) max(coo) min(dat) max(dat)];
19  screenSize = get(0,'ScreenSize');
20
21  figure('Position',[1 1 scrsz(3)/1.8 scrsz(4)/2])
22  errorbar(coo,dat,sdv,'r.')
23  hold on
24  axis([extrema(1)-2 extrema(2)+2 extrema(3)-2 extrema(4)+2])
25  xlabel('Scan [\mum]')
26  ylabel('ADC-values (mean)')
27  title('Focal Edge')
28  coo_contin = extrema(1)-3:0.01:extrema(2)+3;
29
30
31  % Determination of side
32  if dat(1) > dat(length(dat))
33          side = 'left';
34  else
35          side = 'right';
36  end
37
38  % Fitting of error function
39  if side == 'left'
40          start_para = [dat(1)-dat(length(dat)), ...
41          dat(length(dat)), (coo(1)+ ...
42          coo(length(coo)))/2, 1];
43          [f para check iter corr_para cov_para] = ...
44          leasqr(coo', dat, start_para,'edge_left',...
45          0.00001,2000,1./sig);
46          plot(coo_contin, edge_left(coo_contin,para),'k-')
47  else
48          start_para = [-(dat(1)-dat(length(dat))), ...
49          dat(length(dat)), (coo(1)+...
50          coo(length(coo)))/2, 1];
51          [f para check iter corr_para cov_para] = ...
52          leasqr(coo', dat, start_para,'edge_right',...
53          0.00001,2000,1./sig);
54          plot(coo_contin, edge_right(coo_contin,para),'k-')
55  end
56  para_err = sqrt(diag(cov_para));
57  saveas(gcf,['FE',sprintf('%d',measurement), ...
```

```matlab
58 '.',save_format])
59
60
61 % Calculating 1−dim laser profile
62 profiValues = diff(dat)./diff(coo);
63 profiValues = [diff(1);profiValues;diff(length(diff)];
64 pointValues = diff(coo);
65 pointValues = [extrema(1)−3;pointValues;extrema(2)+2]
66 figure('Position',[1 1 scrsz(3)/1.8 scrsz(4)/2])
67 profiContin = para(1)/(sqrt(2*pi)*para(4)) * ...
68 exp(−(coo_contin−para(3)).^2/(2*para(4)^2));
69 plot(pointValues,profiValues,'b−')
70 hold on
71 plot(coo_contin,profiContin,'r−')
72 axis([extrema(1)−2 extrema(2)+2 min(profiContin)−2 ...
73 max(profiContin)+2])
74 xlabel('Scan␣[\mum]')
75 ylabel('Intensity')
76 title('Laser␣profile')
77 saveas(gcf,['P1',sprintf('%d',measurement),...
78 '.',save_format])
79
80 % Calculatin 2−dim laser profile
81 x_cord = −20:0.5:20;
82 y_cord = −20:0.5:20;
83 x_arr = meshgrid(x_cord,y_cord);
84 y_arr = meshgrid(y_cord,x_cord);
85 z_arr = para(1)/(sqrt(2*pi)*para(4)) * ...
86 exp(−(x_arr.^2+y_arr.^2)/(2*para(4)^2);
87 figure('Position',[1 1 scrsz(3)/1.8 scrsz(4)/2])
88 mesh(x_arr,y_arr',z_arr)
89 hold on
90 xlabel('x−Coord.␣[\mum]')
91 ylabel('y−Coord.␣[\mum]')
92 zlabel('Intensity')
93 axis([min(x_cord),max(x_cord),min(y_cord),max(y_cord),...
94 0,max(z_arr)+2])
95 saveas(gcf,['P2',sprintf('%d',measurement),...
96 '.',save_format])
```

edgeleft.m The MATLAB-function `edgeleft.m` describes the signal profile over a left edge of a covering device.

Input: Position
Parameters: [Amplitude, Offset, center of dropdown, width of dropdown]
Output: Signal
Code:

Listing 4: edgeleft.m: Function describing left edges

```
%%% Error Function for Focus Edge (left)

function F = edgeleft(x,p)
%p(1) = amp   p(2) = offset    p(3) = mu   p(4) = sig
F = p(1)*(1-erf((x-p(3))/(sqrt(2)*p(4))))+p(2);
```

edgeright.m The MATLAB-function `edgeright.m` describes the signal profile over a right edge of a covering device.

Input: Position
Parameters: [Amplitude, Offset, center of dropdown, width of dropdown]
Output: Signal
Code:

Listing 5: edgeright.m: Function describing right edges

```
%%% Error Function for Focus Edge (right)

function F = edgeright(x,p)
%p(1) = amp   p(2) = offset    p(3) = mu   p(4) = sig
F = p(1)*(erf((x-p(3))/(sqrt(2)*p(4))))+p(2);
```

D Graphics

This appendix contains all relevant plots in relation to the focus alignment measurements including the error function fits, the plots of $\mu(z)$ and $\sigma(z)$ as well as all reconstructed laser beam profiles.
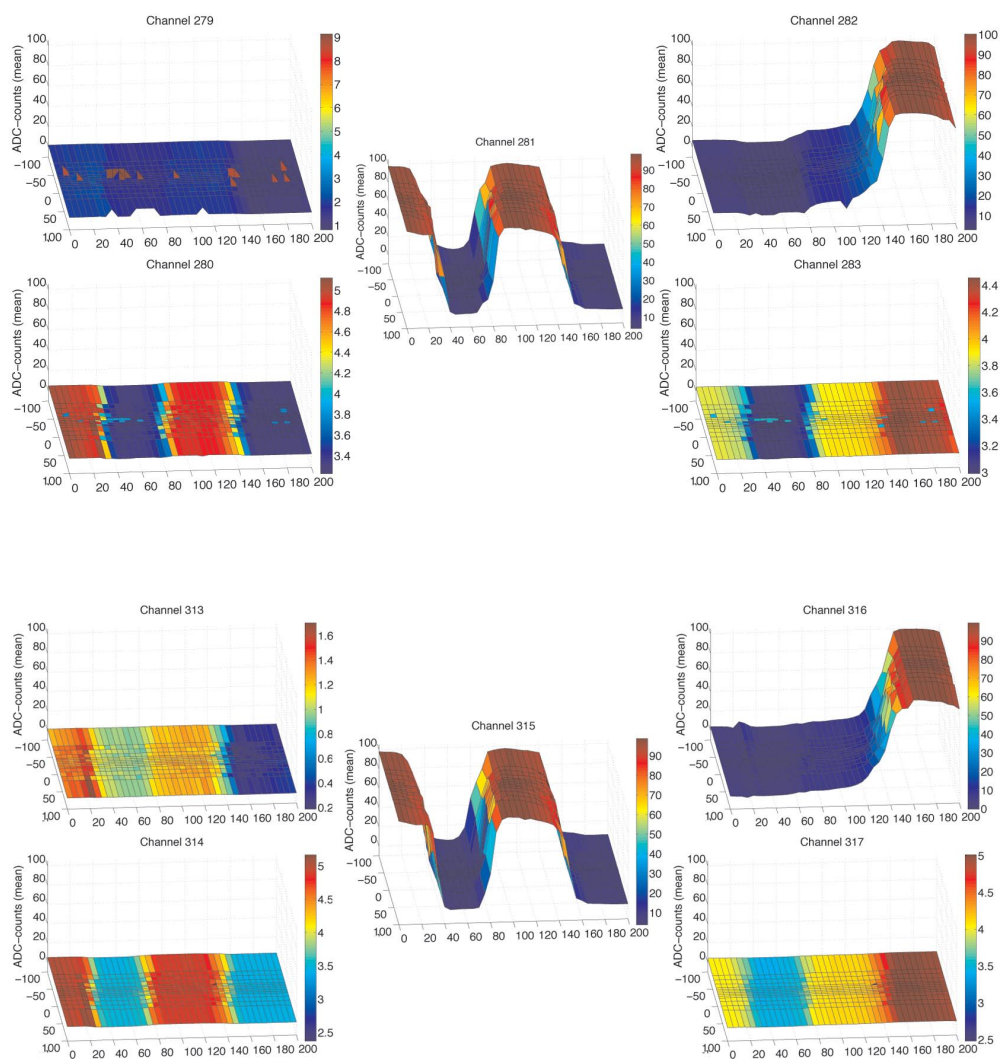

Figure 60: Surface plots of the entire focus measurement. The top group are the channels 313 to 317 (from top left to down right) whereas the bottom group are the channels 279 to 283. The axes are the x-axis ("Scan"; left to right) and z-axis ("Focus"; back to front).
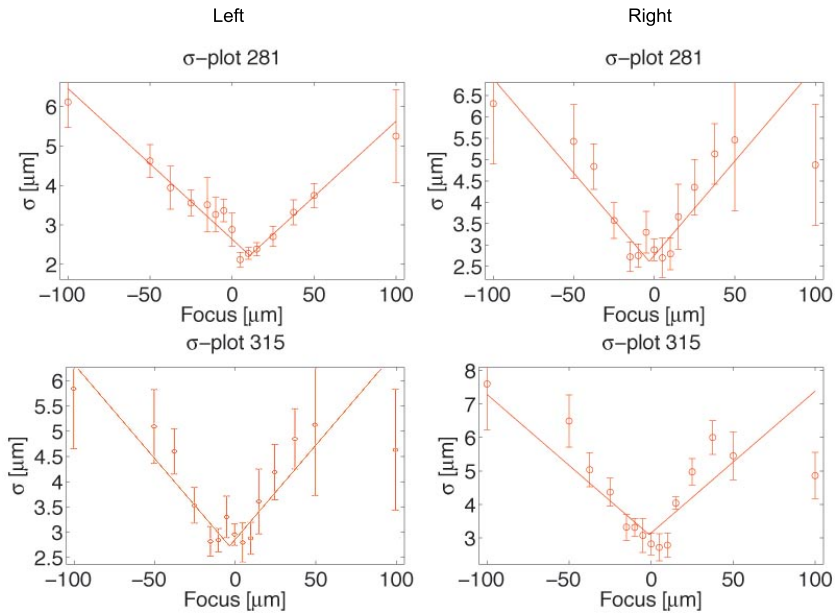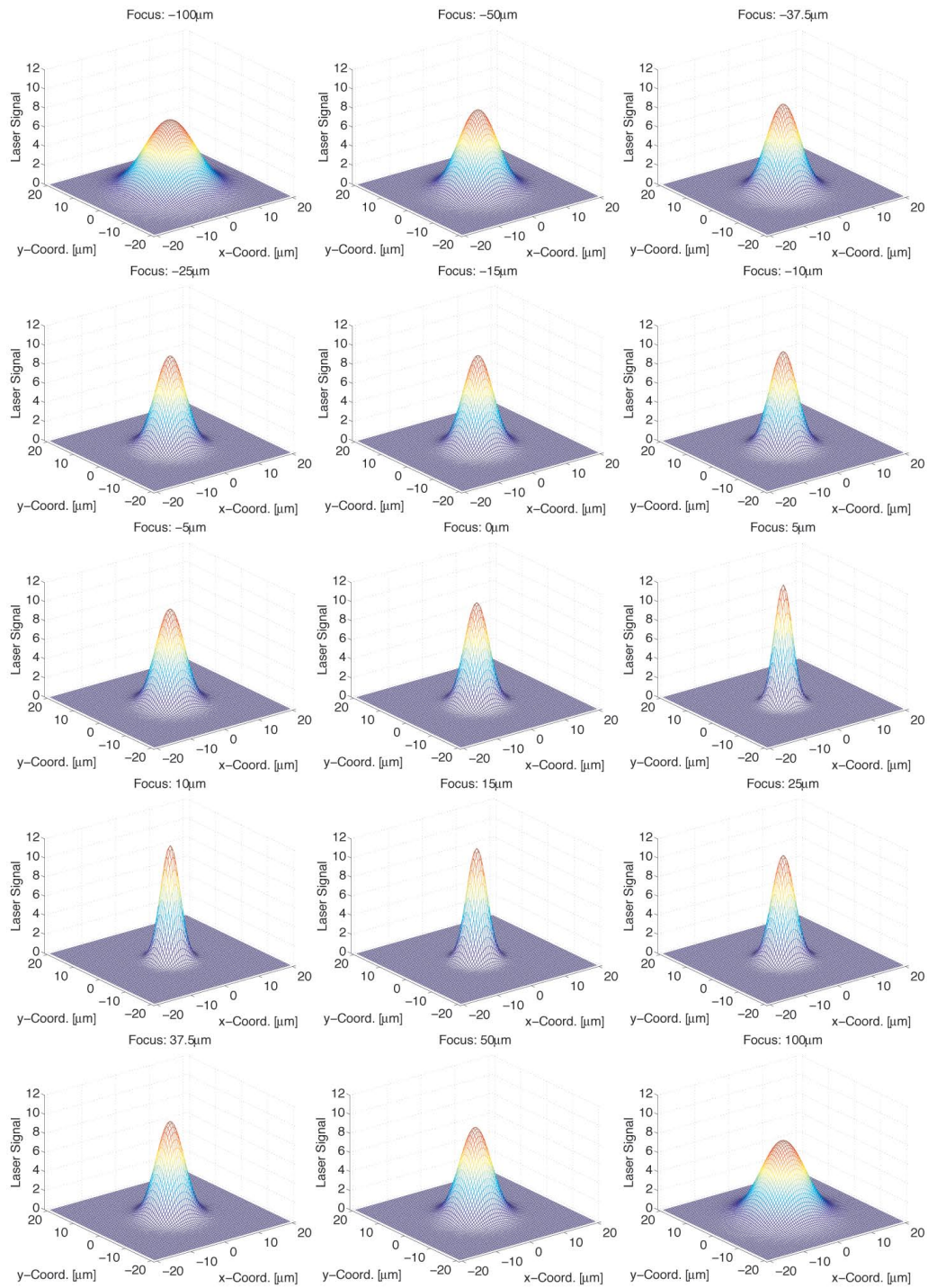
Figure 61: Plots and fits of $\sigma(z)$ for left and right edges of readout strips on 281 and 315
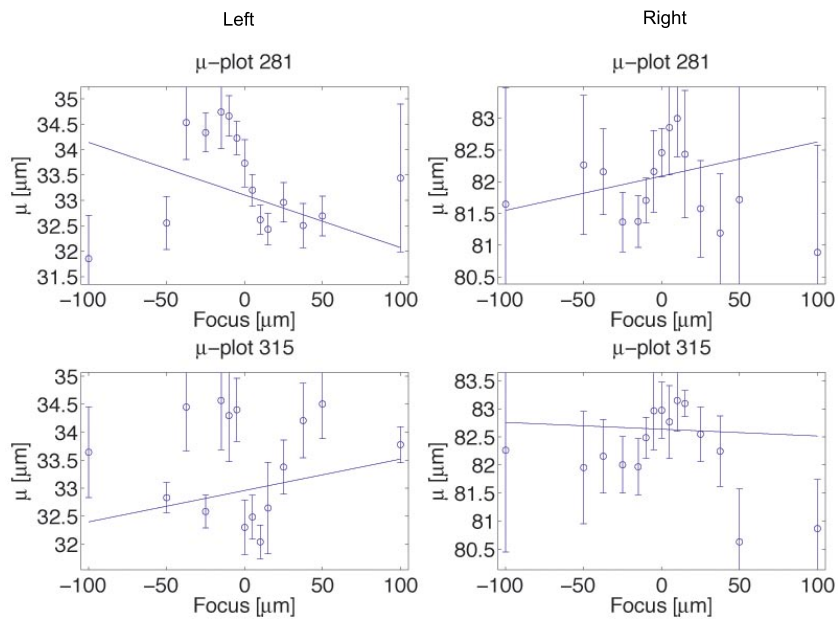
Figure 62: Plots and fits of $\mu(z)$ for left and right edges of readout strips on 281 and 315
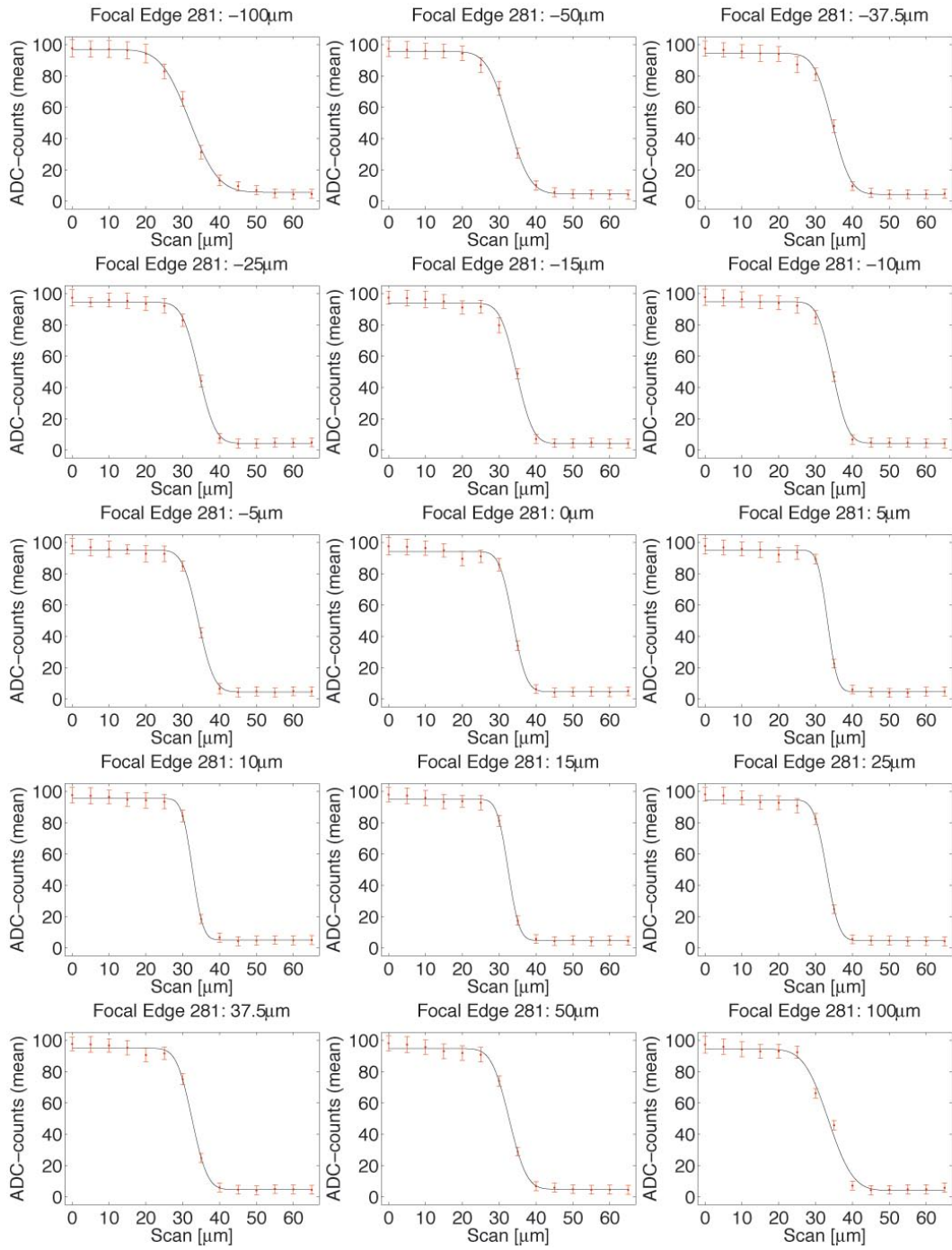
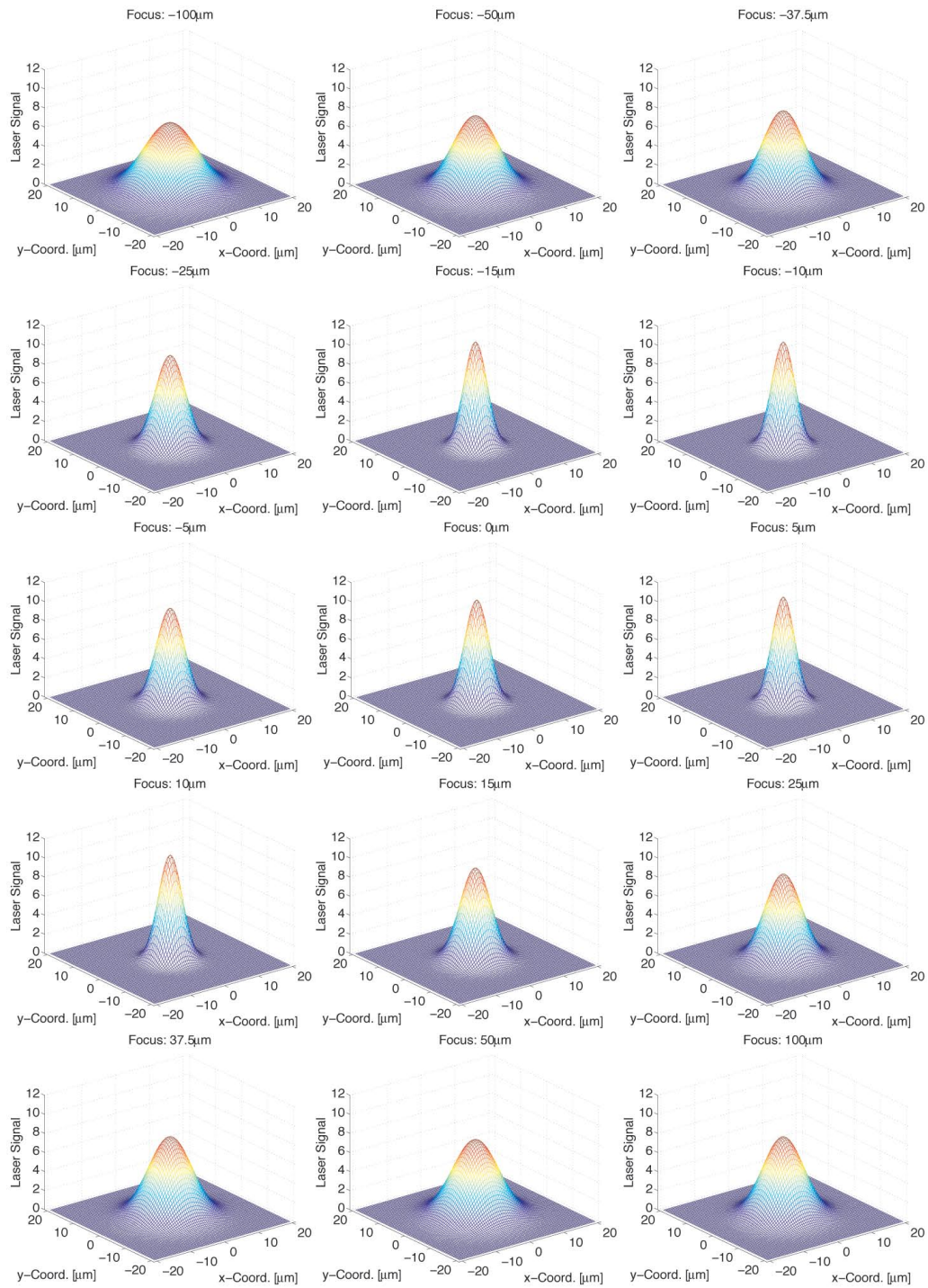**Figure 63:** Plots and fits of all profiles over the left edge of channel 281

74

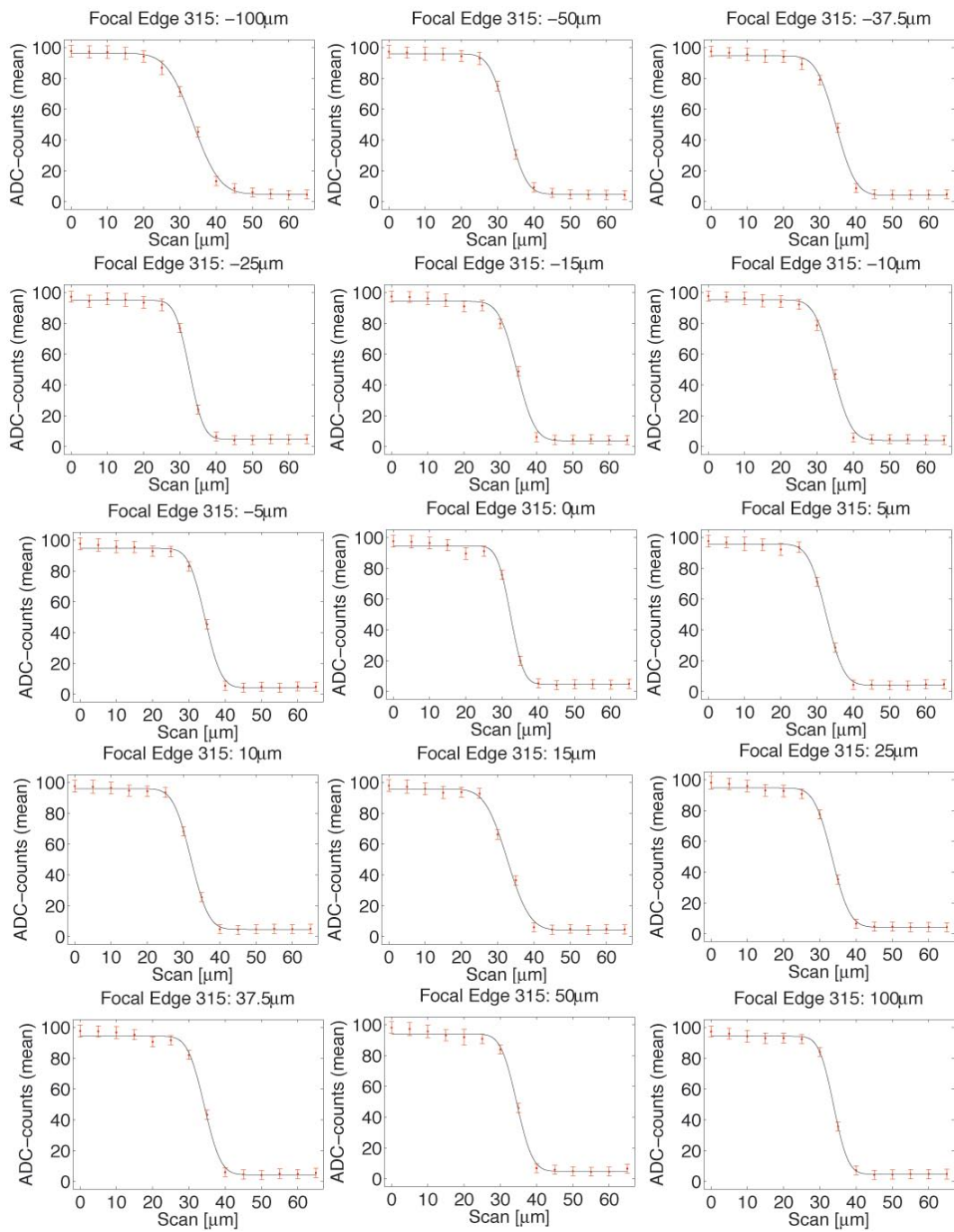**Figure 64:** All reconstructed beam profiles from the left edge of channel 281
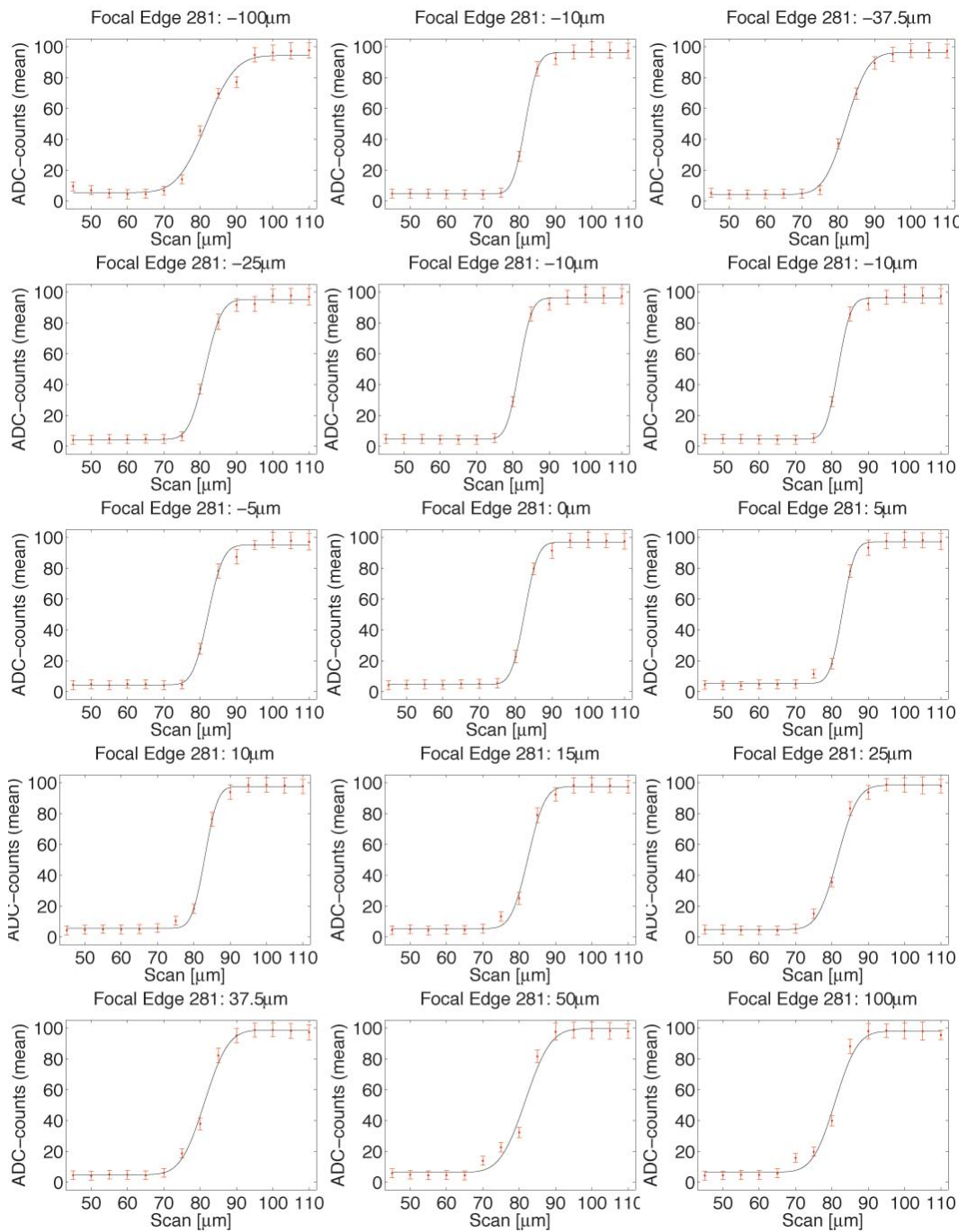
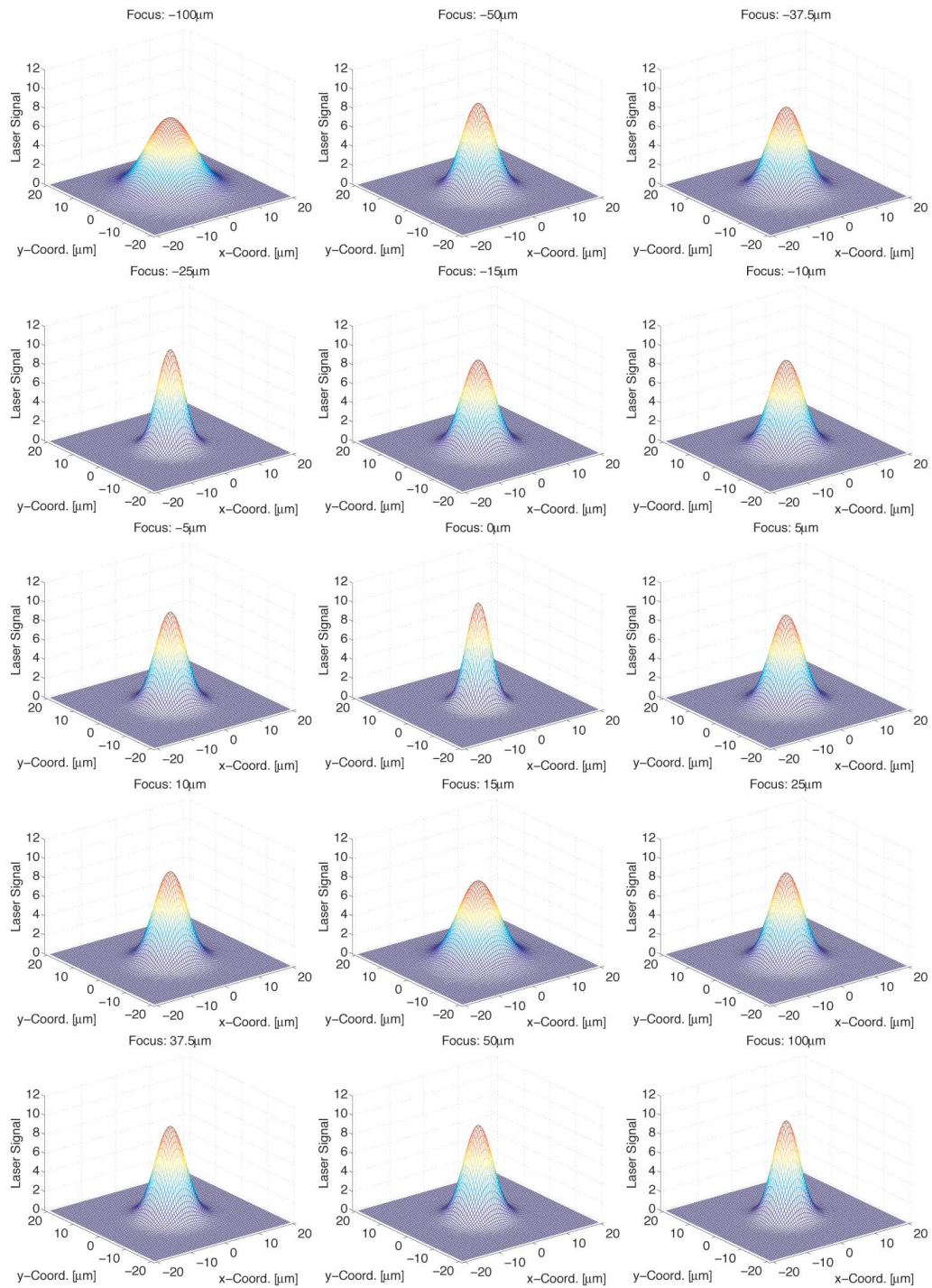**Figure 65:** Plots and fits of all profiles over the right edge of channel 281

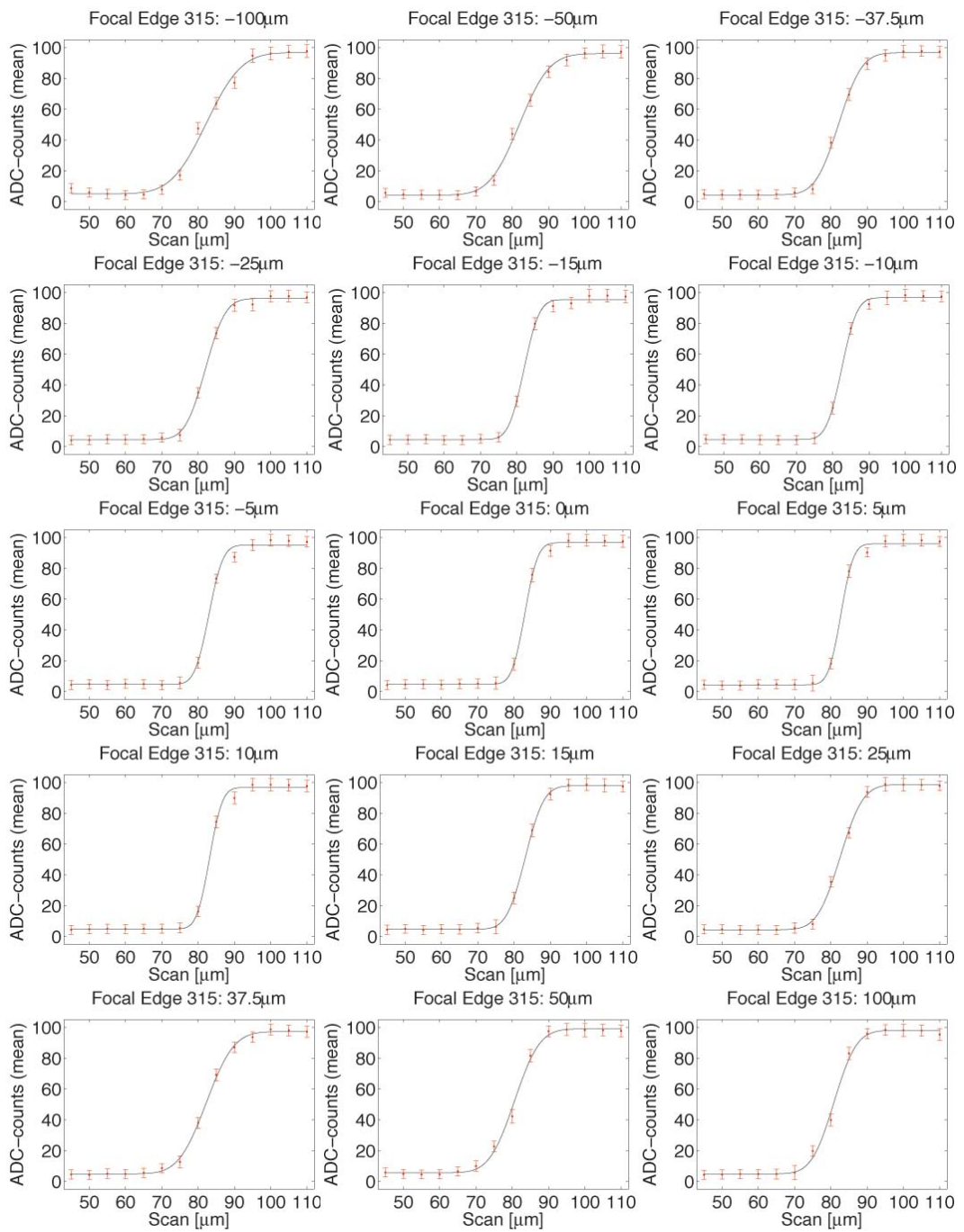**Figure 66:** All reconstructed beam profiles from the right edge of channel 281

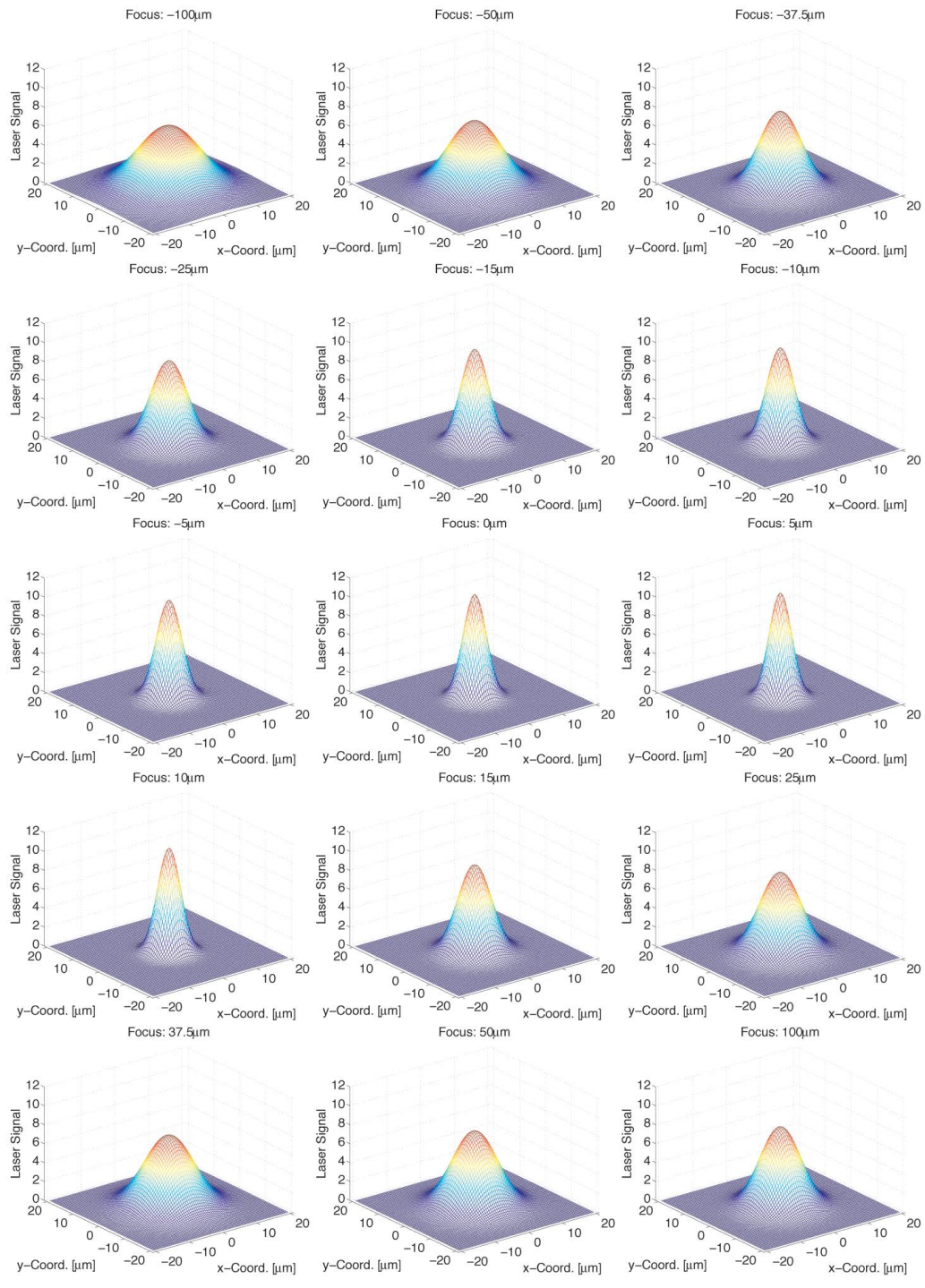**Figure 67:** Plots and fits of all profiles over the left edge of channel 315

Figure 68: All reconstructed beam profiles from the left edge of channel 315

Figure 69: Plots and fits of all profiles over the right edge of channel 315

Figure 70: All reconstructed beam profiles from the right edge of channel 315